

ORIGINAL PAPER

Open Access



Ion microprobe dating of fissure monazite in the Western Alps: insights from the Argentera Massif and the Piemontais and Briançonnais Zones

Emmanuelle Ricchi^{1*} , Edwin Gnos², Daniela Rubatto^{3,4}, Martin John Whitehouse⁵ and Thomas Pettke³

Abstract

Ion probe $^{208}\text{Pb}/^{232}\text{Th}$ fissure monazite ages from the Argentera External Massif and from the high-pressure units of the Western Alps provide new insights on its Cenozoic tectonic evolution. Hydrothermal monazite crystallizes during cooling/exhumation in Alpine fissures, an environment where monazite is highly susceptible to fluid-mediated dissolution-(re)crystallization. Monazite growth domains visualized by BSE imaging all show a negative Eu anomaly, positive correlation of Sr and Ca and increasing cheralite component (Ca + Th replacing 2REE) with decreasing xenotime (Y) component. The buttonite component (Th + Si replacing REE and P) is very low. Growth domains record crystallization following chemical disequilibrium in a fissure environment, and growing evidence indicates that they register tectonic activity. Fissure monazite ages obtained in this study corroborate previous ages, recording crystallization at ~ 36 Ma, $\sim 32\text{--}30$ Ma, and $\sim 25\text{--}23$ Ma in the high-pressure regions of the Western Alps, interpreted to be respectively related to top-NNW, top-WNW and top-SW thrusting in association with strike-slip faulting. During this latter transpressive phase, younger fissure monazite crystallization is recorded between ~ 20.6 and 14 Ma in the Argentera Massif, interpreted to have occurred in association with dextral strike-slip faulting related to anticlockwise rotation of the Corsica-Sardinia Block. This strike-slip activity is predating orogen-parallel dextral strike-slip movements along and through the internal part of all other External Crystalline Massifs (ECM), starting only at ~ 12 Ma. Our combined compositional and age data for hydrothermal monazite track crystallization related to tectonic activity during unroofing of the Western Alps for over more than 20 million years, offering chronologic insights into how different tectonic blocks were exhumed. The data show that fissures in the high-pressure units formed during greenschist to amphibolite facies retrograde deformation, and later in association with strike-slip faulting.

Keywords: $^{208}\text{Pb}/^{232}\text{Th}$ fissure monazite age, Western Alps, High pressure, Argentera Massif, Tectonic activity, Hydrothermal monazite chemistry

1 Introduction

Thorium-Pb dating of hydrothermal monazite-(Ce), hereafter called monazite, offers the possibility to constrain deformation along the retrograde path of a cooling orogen. Recent studies conducted in several parts of the Alpine chain and in the Mexican orogen have acquired numerous Th-Pb monazite crystallization ages that have proven complementary to published chronological and thermochronological data (Bergemann et al. 2017, 2018,

Editorial handling: Paola Manzotti.

*Correspondence: emmanuelle.ricchi@unige.ch

¹ Department of Earth Sciences, University of Geneva, Rue des Maraîchers 13, 1205 Geneva, Switzerland

Full list of author information is available at the end of the article

2019, 2020; Berger et al. 2013; Fitz-Diaz et al. 2019; Gasquet et al. 2010; Gnos et al. 2015; Grand'Homme et al. 2016a; Janots et al. 2012; Ricchi et al. 2019, 2020). Hydrothermal (or fissure) monazite, a Light Rare Earth Element (LREE) phosphate ($(\text{LREE}^{3+}, \text{Th}^{4+}, \text{U}^{4+})\text{P}^{5+}\text{O}^{2-}_4$) that is commonly mm-sized, crystallizes in fluid-filled Alpine-type fissures in a temperature range of ~ 400 – 200 °C (Gnos et al. 2015; Janots et al. 2019). Alpine fissures form at P-T conditions at or below 0.3–0.4 GPa lithostatic pressure and 450–500 °C (e.g. Mullis 1996; Sharp et al. 2005; Stalder et al. 1998). The fissures are usually oriented perpendicular to the main foliation and lineation of the host-rock (e.g. Gnos et al. 2015). When a fissure opens and becomes filled by aqueous fluid, chemical disequilibrium between the fluid and host-rock wall leads to dissolution of host-rock wall minerals, resulting in a porous and commonly bleached alteration envelope (e.g. Gnos et al. 2015). Within the fissure, this results in the crystallization of strongly zoned hydrothermal minerals. The dissolution and reprecipitation of fissure minerals is generally a cyclic process triggered when chemical disequilibrium occurs, commonly related to tectonic activity (e.g. fissure propagation, exposure or delamination of fissure wall).

In monazite-bearing fissures, quartz and adularia typically form at an early stage of fissure formation (<500–450 °C), whereas monazite crystallizes at later stages (between 400–200 °C) (e.g. Gnos et al. 2015). Thus, monazite dating does not yield the formation of the fissure but only subsequent stages of hydrothermal activity, usually caused by deformation under greenschist to sub-greenschist facies metamorphic conditions.

Fissure monazite is reliably dated by the ^{232}Th - ^{208}Pb system, as it typically incorporates high Th contents (e.g. Janots et al. 2012) and no Pb (e.g. Gardés et al. 2007) during its crystallization. Moreover, Th and Pb diffusion are negligible under hydrothermal monazite crystallization conditions (<400 °C) due to the high closure temperature of monazite (>800 °C; e.g. Cherniak et al. 2004; Cherniak and Pyle 2008; Gardés et al. 2006, 2007). The ^{232}Th - ^{208}Pb isotopic system can thus only be disturbed or reset by chemical disequilibrium induced by the presence of hydrous fluids resulting in the dissolution and/or re-precipitation of monazite (e.g. Cherniak et al. 2004; Cherniak and Pyle 2008; Grand'Homme et al. 2016b; Seydoux-Guillaume et al. 2002, 2012), a process that commonly

results in patchy monazite replacing prior monazite (e.g. Grand'Homme et al. 2016b). Each dissolution, replacement or growth of a monazite domain corresponds to a reaction induced by chemical disequilibrium, which might be related to deformation events (see above), and can usually be identified texturally (e.g. patchy texture, growth zoning, cross cutting relationships) and chemically (distinct Th/U ratio; e.g. Grand'Homme et al. 2016a; Grand'Homme et al. 2016b; Seydoux-Guillaume et al. 2012). Thus, dating of hydrothermal monazite growth domains within a single sample has the potential to identify a sequence of tectonic events.

Previous studies on fissure monazite grains from the French parts of the Western Alps have provided weighted mean ages between 11.6 ± 0.3 and 6.7 ± 0.2 Ma in the Mont-Blanc Massif (Bergemann et al. 2019; Grand'Homme et al. 2016a), between 9.2 ± 0.3 and 7.9 ± 0.3 Ma in the Aiguilles Rouges Massif (Bergemann et al. 2019), between 12.4 ± 0.1 and 5.4 ± 0.5 Ma in the Belledonne Massif (Gasquet et al. 2010; Grand'Homme et al. 2016a), 17.6 ± 0.3 Ma in the Pelvoux Massif (Gasquet et al. 2010), 20.6 ± 0.3 Ma in the Argentera Massif (Grand'Homme et al. 2016a) and 23.0 ± 0.3 and of 32.3 ± 0.3 Ma in the Briançonnais Zone (Grand'Homme et al. 2016a; Fig. 1).

This study was undertaken in order to confirm with supplementary data that fissure monazites in the Argentera Massif and the Piemontais and Briançonnais zones are older than monazites from other parts of the Western Alps. Fissures are relatively rare in these parts of the Alps. For this reason, only five fissure monazites were available for this study (Table 1). In addition to backscatter electron images, we also tried to use trace and rare earth elements to distinguish growth domains in the monazites.

2 Geological setting

The Western Alps are the result of the closure of the Ligurian part of the Tethys and the collision of the European with the Apulian plate (e.g. Lemoine et al. 1986; Schmid et al. 2004). This process lasted from the Cretaceous to the Eocene (e.g. Rubatto et al. 1999; Rubatto and Hermann 2001; Table 2).

This study focuses on the westernmost part of the Alps, an arcuate and roughly N-S oriented segment of the Alpine orogen characterized by the exposure of European (or external) units in the west, separated tectonically

(See figure on next page.)

Fig. 1 Tectonic map of the study area modified after Schmid et al. (2004), Sanchez et al. (2011a), Steck et al. (2013) and Bergemann et al. (2019). Stars correspond to monazite samples from this study (yellow) and from Gasquet et al. (2010), Grand'Homme et al. (2016a) and Bergemann et al. (2019) (green stars). Weighted mean age or age range of growth domains in monazite are indicated. The internal domains are labelled as follow: MR: Monte Rosa, DB: Dent Blanche, S: Sesia, GP: Grand Paradiso, Am: Ambin, DM: Dora Maira

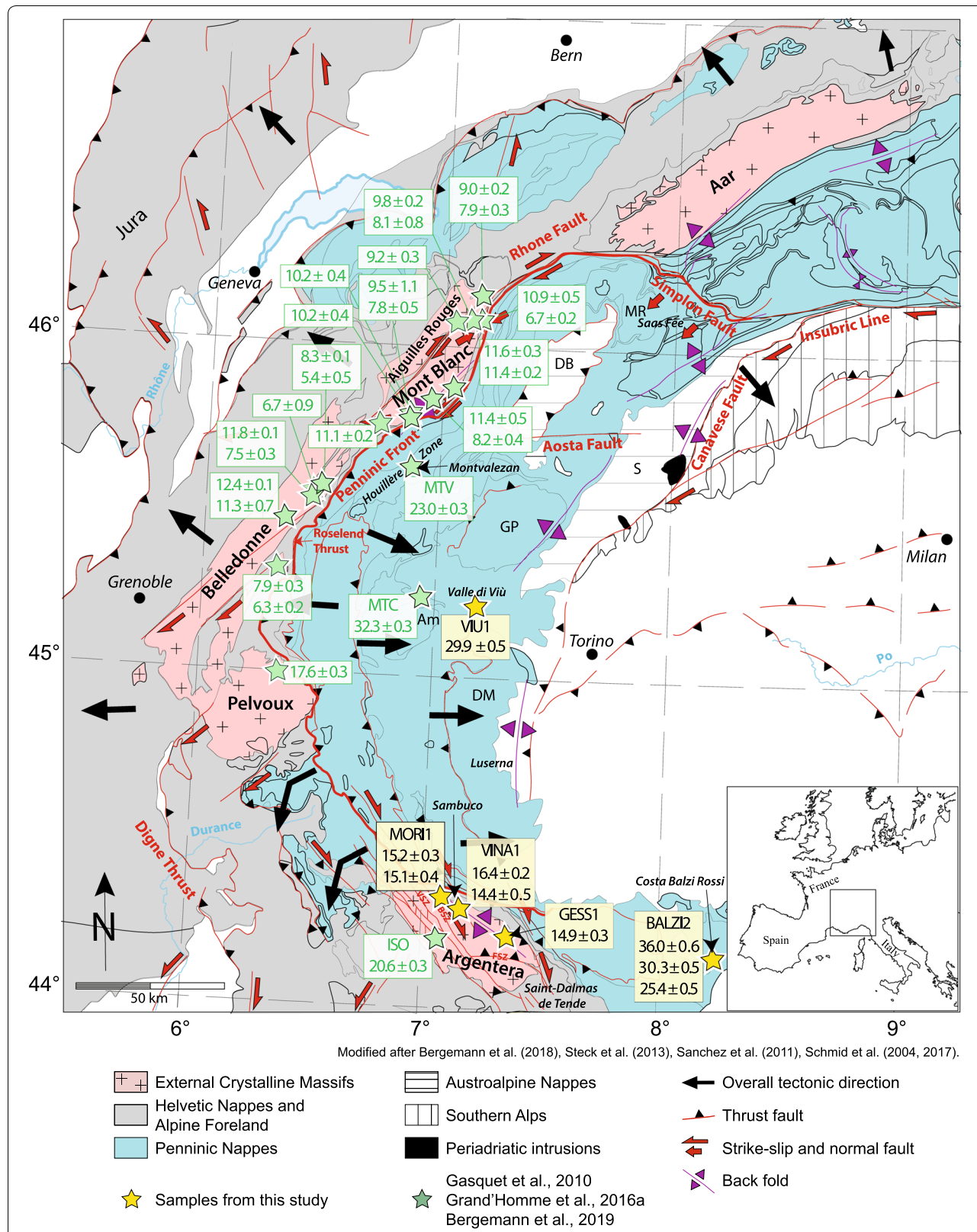


Table 1 Summary of monazite-(Ce) samples considered in this study with information on sample locality, host-rock lithology and metamorphic degree, fissure mineral association and orientation

Locality	Sample	Domain	Latitude (°N)	Longitude (°E)	Host-rock	Alpine metamorphism	Association	Average fissure orientation
Margone, Valle di Viù, Piedmont, Italy	VIU1	Piémontais Zone	45°13.064'	007°11.268'	gneiss	Eclogite/green-schist facies	Qz, Ab, Rt	181/77
Costa Balzi Rossi, Magliolo, Liguria, Italy	BALZI2	Briançonnais Zone	44°11.300'	008°14.100'	metarhyolites	Blueschist/green-schist facies	Qz, Ab, Ad, Ant, Brk, Hem, Xnt	Block in scree
Morglione, Valle Stura, Argentera, Piedmont, Italy	MORI1	Argentera Massif	44°20.470'	007°04.767'	gneiss	Greenschist facies	Qz, Ad, Ant	186/86
Vinadio, Valle Stura, Argentera, Piedmont, Italy	VINA1	Argentera Massif	44°18.376'	007°09.606'	gneiss	Greenschist facies	Qz, Ad, Ant	186/86
Monte Ray, Valle Gesso, Entraque, Piedmont, Italy	GESS1	Argentera Massif	44°13.660'	007°21.640'	gneiss	Greenschist facies	Cc, Ant, Syn, Xnt, Crt	Vertical

Ab albite, Ad adularia, Ant anatase, Brk brookite, Cc calcite, Crt cerussite, Hem hematite, Qz quartz, Rt rutile, Syn synchisite-(Ce), Xnt xenotime-(Y)

from Penninic (or internal) units by the Penninic Front (PF) (Fig. 1). The external crystalline massifs (ECM) derive from the European margin and consist of the Aar, Gotthard, Mont Blanc, Aiguilles Rouges, Belledonne, Pelvoux and Argentera massifs and their corresponding sedimentary cover (Helvetic and Dauphiné units), whereas the internal units formed during subduction-collision of the Tethyan Ocean and the European margin and consists of lower and middle Penninic units (Valais and Briançonnais Zones) and upper Penninic units (Piemontais, Schistes Lustrés and Austro-Alpine Units; Fig. 1; e.g. Ceriani et al. 2001; Schmid et al. 2004). The different units of the Piemontais and Briançonnais Zones show Alpine eclogite/greenschist and blueschist/greenschist metamorphism, whereas the Argentera and other external Massifs show greenschist facies metamorphism (Bousquet et al. 2012).

In the external Alps, shortening started during the main collisional phase of the orogen, at the transition between the Late Eocene and the Early Oligocene (Ceriani et al. 2001). According to that study, the boundary between the external and internal units (the PF) acted first as a transpressive suture zone that became sealed by Priabonian flysch. This first activation of the PF, related to the underthrusting of the ECM below the internal units, occurred in the Eocene and ended at ~35 Ma (e.g. Ceriani et al. 2001; Grand'Homme et al. 2016a; 1st episode/stage on Table 2). It was then reactivated between 35 and 25 Ma according to Schmid et al. (2017), where it acted as a WNW-directed thrust: the Roselend Thrust. At

larger scale, this indicates an oblique (sinistral) collision during the Eocene, followed by westward indentation of the Ivrea mantle wedge (portion of the Adria mantle lithosphere), associated with backfolding and back-thrusting (e.g. Ceriani et al. 2001; Collombet et al. 2002; Schmid et al. 2017; 2nd episode/stage on Table 2). This indentation overprinted the Eocene regime of sinistral transpression in the area of the Western Alps (Laubscher 1991) and was followed by a Miocene shortening phase related to the exhumation of the ECM (Table 2). During the Neogene, orogen-parallel deformation developed at the expense of NW-directed thrusting (e.g. Hubbard and Mancktelow 1992). This NE-trending deformation was associated with extensional movements along the Simplon normal fault due to exhumation of the Leptonine structural and metamorphic dome (e.g. Bergemann et al. 2020), accommodated by dextral strike-slip faults, bordering and cutting the ECM, and by SW-directed thrusting along the Digne Thrust (Table 2). The top-SW thrusting affecting the southern part of the Western Alps is related to the formation of the Apennines leading to oroclinal bending. Simultaneously, anticlockwise rotation of the Corsica-Sardinia block between 20.5 and 16 Ma accommodates the opening of the Liguro-Provençal Basin (Gattacceca et al. 2007; Maffione et al. 2008; Schmid et al. 2017; stage 3 on Table 2). From the Pliocene onwards, brittle normal faulting developed following the reactivation of the northern and southern Houiller and Penninic Front (Fügenschuh et al. 1999; 3rd episode of Ceriani et al. 2001, Table 2). Seismological data attest that

Table 2 Summary of deformation phases in the Western Alps

Age [Ma]	Domain	Characteristics	Phase	Monazite age [Ma]	Remarks	Ref
Large-scale deformation history: Cretaceous to Eocene	Western Alps	Subduction of the Thethys Ocean			Related to subduction prism formation, composed of internal Penninic units	K, P, V
Middle to Late Eocene	Western Alps	Subduction of the European continental margin			Related to the exhumation of the internal units and the onset of the external Alps	E, K, Q
Late Eocene to Early Oligocene	Western Alps	European margin—Apulia collision			Related to N-S-directed convergence and frontal collision in the Central Alps; ECM under-thrusted below internal units	B, G, K, S
Eocene to earliest Oligocene ~35	Western Alps	Oblique collision associated to top>NNW thrusting in sinistral transpression; PF activation	1st episode of B / Stage 1 of R		Related to the end of N-S-directed head-on collision in the Central Alps	B, T
35–25	Western Alps	End of oblique collision	End of 1st episode of B		Related to WNW-directed indentation of the Ivrea mantle wedge. Overprint of Eocene sinistral transgression	B, C, R, S
Miocene	Western Alps	Top-WNW-directed thrusting along the PF, associated to backfolding and backthrusting	2nd episode of B / Stage 2 of R		Contemporaneous westwards migration of the deformation front	D, T
Miocene—Pliocene	Western Alps	Shortening phase and exhumation of the ECM			SW-directed normal faulting (Simplon Fault), NE-striking dextral strike-slip (around and through the ECM), SW-directed thrusting (Digne)	F, L
25–0	Southern part of the Western Alps	Orogen-parallel deformation	Stage 3 of R		Related to orogeny in the Apennines and opening of the Liguro-Provençal Basin	J, N, S
After 5	Western Alps	Top-SW thrusting, oroclinal bending and anticlockwise rotation of the Corsica-Sardinia block (20.5–15 Ma)	3rd episode of B		Related to reactivation of the Houiller Front in the N and the Penninic Front in the S	B, G, W
Deformation in the high-pressure units (internal domains): Late Eocene to Oligocene	Briançonnais Zone	Late brittle normal/faulting, orogen-perpendicular extension	D1 to D2 phase of C	~32	Monzage coincides with the exhumation along the PF	C, K

Table 2 (continued)

Age [Ma]	Domain	Characteristics	Phase	Monazite age [Ma]	Remarks	Ref
Late Oligocene	Briançonnais Zone	Back-thrusting (main folding phase)	D3 phase of C	~23	Mnz age is difficult to attribute to a given deformation episode	C, K
Miocene—Actual	Briançonnais Zone	Normal/strike-slip faults (late Alpine tilting)	D4 phase of C			
Deformation in the ECM (external domains); ~22.5	Argentera Massif	First major shortening phase related to shear zone formation (horizontal veins)				D, K
~20–15	Pelvoux Massif	Exhumation and cooling related to thrusting (horizontal veins)		~17.6	Mnz from a horizontal vein records the major uplift of the Pelvoux Massif (horizontal vein)	D, H, I
~11–10 and 7–5	Belledonne Massif	Polyphased transpressive regime and "en échelon" arrangement of vertical veins		~12—5.5	Mnz ages are related to dextral movements along the Ornon-Roselend fault and the Rhône-Simplon fault (vertical veins)	I, K
~23–22 and ~16	Mont Blanc Massif	First and second shortening related to shear zone formation (horizontal veins)		~11.5—6.5	Mnz ages related to NE striking dextral strike slip (vertical vein)	A, K, M, O
	Aiguilles Rouges Massif			~9—8	Mnz ages related to NE striking dextral strike slip (vertical veins)	

A: Bergemann et al. 2019; B: Ceriani et al. 2001; C: Collombet et al. 2002; D: Corsini et al. 2004; E: Duchêne et al. 1997; F: Dumont et al. 2008; G: Fügenschuh et al. 1999; H: Fügenschuh and Schmid 2003; I: Gasquet et al. 2010; J: Gattaccea et al. 2007; K: Grand'Homme et al. 2016a; L: Hubbard and Mancktelow, 1992; M: Leloup et al. 2005; N: Maffone et al. 2008; O: Rossi and Rolland 2014; P: Rubatto et al. 1999; Q: Rubatto and Hermann 2001; R: Schmid et al. 2004; S: Schmid et al. 2017; T: Schmid and Kissling 2000; U: Simon-Labrec et al. 2009; V: Steck et al. 2013; W: Sue 1999; Mnz: monazite; ECM: External Crystalline Massifs; PF: Penninic Front

the Penninic core of the Western Alps is still affected by this orogen-perpendicular extension (Sue et al. 1999).

Whereas the timing of fissure formation in the external massifs (except Argentera) is well constrained by monazite data (Gasquet et al. 2010; Grand'Homme et al. 2016a, b; Bergemann et al. 2019; Ricchi et al. 2019), such data are sparse for the Argentera Massif and the high-pressure overprinted units.

3 Methods

In situ Th-Pb dating of five monazite grains was carried out at the SwissSIMS Ion microprobe facility, equipped with a Cameca IMS 1280 HR instrument, at the University of Lausanne, Switzerland (Table 3). Preliminary sample preparation and backscattered electron (BSE) imaging was conducted for identifying distinct chemical and textural domains, following the procedure of Bergemann et al. (2017). The SIMS spot measurements were distributed on the basis of domains visible to capture the crystallization duration. In order to obtain more robust growth domain ages, the selected domains were large enough to place a minimum of three measurement spots. The instrument was run using the same procedure as Janots et al. (2012) and the same parameters as Ricchi et al. (2019, 2020). The SIMS measurements were performed focusing a -13 kV O₂⁻ primary beam on the samples with an intensity of ca. 3nA creating a spot with a 15 µm diameter. Applying a mass resolution between 4300–5000 depending on analytical session ($M/\Delta M$, at 10% peak height) and an energy window at 40 eV, with data collected in peak hopping mode using an ion-counting electron multiplier. USGS-44069 monazite (425 Ma; Aleinkoff et al. 2006) was selected to standardise the data; the uncertainty on the standard ²⁰⁸Pb/²³²Th–ThO/Th calibration was between 1.01 to 2.56%. Data reduction and standardization was also carried out using the same parameters as Ricchi et al. (2020); namely, common lead Pb_c correction was calculated at time zero applying the terrestrial Pb evolution model of Stacey and Kramers (1975) using the Cameca Customisable Ion Probe Software (CIPS) and Isoplot 4.15 (Ludwig 2003) software. Isoplot 4.15 was also employed for weighted average age calculations and plotting. Uncertainties on single ages are quoted at 1 sigma level and weighted mean ages, hereafter called average ages, are quoted at 95% confidence level throughout the text (Table 4).

Previous studies have shown that U-Th contents seem to be the easiest way to differentiate domains and to identify altered zones (e.g., Gnos et al. 2015; Bergemann et al. 2017). Since new crystallization or alteration is associated with a change in chemical composition and likely happened in equilibrium with the surrounding fluid, any age cluster within a chemical group must be due to the simultaneous formation or alteration of those monazite parts.

Spatially close BSE regions displaying a comparable grey shade, showing chemical grouping and providing comparable age spots are treated as one growth domain. Some domains were too small to provide robust average ages, and single spot ages may still provide hints about the crystallization history. Weighted mean ²⁰⁸Pb/²³²Th ages were calculated for each growth domain following the approach of Bergemann et al. (2017, 2018, 2019, 2020) and Ricchi et al. (2019, 2020). Since fissure monazite is dissolved and re-precipitated under changing chemical conditions (e.g. Grand'Homme et al. 2018), spot analyses affected by Pb_c (as indicated by older dates related to higher Pb_c, i.e. positive age-f₂₀₈ correlation), or those with high uncertainty (1σ absolute > 1) were removed from the dataset. However, analyses located on dissolution trails, generally providing younger dates, were considered in the age ranges because they likely record a later phase of monazite alteration.

Laser-Ablation Inductively-Coupled-Plasma Mass-Spectrometry (LA-ICP-MS) analyses were carried out to obtain the concentration of major and trace elements in the investigated fissure monazites (Table 5). The measurements were done using a GeoLas-Pro 2006 193 nm ArF Excimer laser system (Lambda Physik / Coherent) interfaced to a Perkin Elmer Elan DRC-e quadrupole mass spectrometer at the University of Bern. The ablation was performed following procedures as documented in Bergemann et al. (2017) and Gnos et al. (2015), using beam sizes of 24 to 60 µm to measure as close as possible to the ion probe spots in the same growth domain, with an energy density on the sample of 4–5 J/cm² and a laser repetition rate of 10 Hz. The ICP-MS settings were optimized to maximum signal to background intensity ratios with (²³²Th¹⁶O)⁺ production rates tuned to below 0.2% and robust plasma conditions as monitored by equal sensitivities of U and Th. Two reference materials were used, GSD-1G for external calibration and the synthetic SRM 610 glass from the National Institute of Standards and Technology (NIST) for quality control, employing preferred element concentration data from GeoRem (<https://georem.mmpc-mainz.gwdg.de/>). Data quantification used total oxides for internal standardisation (i.e., summation of the measured major element oxides (P₂O₅, CaO, Y₂O₃, La₂O₃, Ce₂O₃, Pr₂O₃, Nd₂O₃, Sm₂O₃, Eu₂O₃, Gd₂O₃, Tb₂O₃, Dy₂O₃, ThO₂) to 100 wt%; e.g. Gray 1985). Data reduction was performed using the SILLS software (Guillong et al. 2008) with improved calculation of the limit of detection (Pettke et al. 2012).

4 Results

4.1 Alpine fissures in the Western Alps

Two fissure monazites analysed in this study were collected in the high-pressure regions of the Western Alps, sample VIU1 is from the Piemontais Zone (eclogite/

Table 3 Ion microprobe Th-U-Pb analyses of fissure monazite

Groups	Analysis ID	U (μg/g)	Th (μg/g)	Th/U	$^{208}\text{Pb}/^{204}\text{Pb}$	$^{207}\text{Pb}/^{204}\text{Pb}$	1σ (%)	$^{207}\text{Pb}/^{206}\text{Pb}$	1σ (%)	$^{208}\text{Pb}/^{232}\text{Th}$	1σ (%)	f208 from 207(%)	204—corr	204—corr spot ages		207—corr	207—corr spot ages		
														$^{208}\text{Pb}/^{232}\text{Th}$	1σ (%)	$^{208}\text{Pb}/^{232}\text{Th}$	1σ (%)	Age (Ma)	
high-pressure regions																			
A	VIU@01	42,000	108	2739	8	0.078	20	0.001576	1.5	0.3	0.001554	1.5	31.38	0.47	0.001571	1.5	31.73	0.49	
	VIU@02	31,000	94	3335	10	0.071	23	0.001518	1.5	0.3	0.001501	1.5	30.31	0.46	0.001514	1.5	30.58	0.47	
	VIU@03	230	26,000	113	3274	11	0.087	25	0.001537	1.5	0.4	0.001519	1.5	30.69	0.47	0.001531	1.5	30.92	0.47
	VIU@04	330	36,000	109	2810	9	0.082	21	0.001611	1.5	0.4	0.001589	1.5	32.09	0.49	0.001605	1.5	32.42	0.50
	VIU@06	250	28,000	112	2499	11	0.100	24	0.001655	1.5	0.6	0.001630	1.5	32.91	0.50	0.001645	1.5	33.21	0.51
	VIU@11	240	22,000	92	2261	11	0.120	21	0.001622	1.5	0.9	0.001594	1.5	32.20	0.49	0.001607	1.5	32.46	0.50
	VIU@05	280	19,000	68	1588	10	0.128	21	0.001485	1.5	1.2	0.001449	1.5	29.27	0.44	0.001468	1.5	29.64	0.45
	VIU@07	310	17,000	55	2116	14	0.093	25	0.001457	1.5	0.9	0.001431	1.5	28.91	0.44	0.001444	1.5	29.16	0.45
	VIU@08	320	21,000	66	2545	14	0.094	25	0.001483	1.5	0.8	0.001460	1.5	29.50	0.45	0.001471	1.5	29.77	0.46
	VIU@09	310	17,000	55	2893	16	0.085	26	0.001508	1.5	0.8	0.001488	1.5	30.04	0.46	0.001496	1.5	30.21	0.47
	VIU@10	280	13,000	46	1791	14	0.093	24	0.001563	1.7	1.2	0.001529	1.7	30.88	0.52	0.001544	1.7	31.18	0.53
	VIU@12	240	22,000	91	1686	9	0.184	1.8	0.001548	1.6	1.6	0.001513	1.5	30.55	0.47	0.001523	1.6	30.76	0.48
	VIU@13	270	14,000	52	2582	14	0.110	24	0.001493	1.5	1.1	0.001471	1.5	29.71	0.45	0.001477	1.5	29.83	0.46
	VIU@14	250	12,000	48	1564	13	0.121	24	0.001550	1.5	1.4	0.001511	1.5	30.53	0.47	0.001527	1.5	30.85	0.48
	VIU@15	290	14,000	48	1547	13	0.133	24	0.001434	1.6	1.5	0.001398	1.6	28.24	0.45	0.001412	1.6	28.52	0.46
	VIU@16	250	20,000	80	2316	11	0.104	2.2	0.001571	1.5	0.8	0.001546	1.5	31.22	0.47	0.001558	1.5	31.47	0.48
	VIU@17	270	21,000	78	2263	11	0.103	2.3	0.001501	1.6	0.7	0.001475	1.5	29.79	0.46	0.001489	1.6	30.08	0.47
	VIU@18	260	21,000	81	2431	11	0.088	25	0.001524	1.5	0.5	0.001500	1.5	30.29	0.46	0.001516	1.5	30.61	0.47
	VIU@19	290	18,000	62	3043	14	0.091	26	0.001452	1.5	0.6	0.001434	1.5	28.96	0.44	0.001443	1.5	29.14	0.45
	VIU@20	360	17,000	47	2522	13	0.086	26	0.001432	1.6	0.7	0.001412	1.5	28.52	0.44	0.001423	1.6	28.74	0.45
	BALZ12@34	410	2700	7	1299	95	0.141	11.7	0.002080	1.2	4.4	0.002018	3.1	40.74	1.25	0.001988	1.4	40.14	0.57
	BALZ12@36	210	3800	18	938	95	0.374	13.2	0.002306	1.6	7.4	0.002396	5.8	48.38	2.79	0.002135	1.9	43.10	0.81
	BALZ12@37	4600	6	/	0	0.068	244	0.002502	1.1	0.8	0.002502	/	50.50	/	0.002483	1.2	50.12	0.58	
	BALZ12@39	950	7000	7	1341	95	0.119	16.1	0.002273	2.1	2.1	0.002207	3.4	44.56	1.51	0.002225	2.1	44.92	0.95
	BALZ12@40	510	5500	11	744	42	0.174	7.0	0.002073	2.3	4.7	0.001966	3.1	39.69	1.22	0.001975	2.3	39.88	0.91
	BALZ12@42	150	3900	26	594	47	0.340	8.7	0.001922	1.3	6.5	0.001797	3.3	36.29	1.21	0.001796	1.5	36.28	0.53
	BALZ12@43	250	3900	16	/	0	0.074	14.2	0.001774	2.2	0.9	0.001774	/	35.81	/	0.001757	2.2	35.48	0.77
	BALZ12@44	320	3800	12	306	25	0.263	4.6	0.001997	2.5	11.0	0.001745	3.8	35.23	1.33	0.001778	2.6	35.90	0.92
	BALZ12@45	240	4900	20	218	25	0.479	5.1	0.002144	1.1	16.0	0.001764	4.4	35.62	1.58	0.001800	1.3	36.36	0.49
	BALZ12@46	320	5800	18	2020	67	0.089	11.6	0.001749	2.2	1.0	0.001716	2.5	34.65	0.86	0.001731	2.2	34.96	0.76
	BALZ12@47	86	4100	48	704	55	0.336	11.0	0.001741	1.0	4.6	0.001646	3.2	33.24	1.05	0.001661	1.1	33.55	0.37

Table 3 (continued)

Groups	Analysis ID	U ($\mu\text{g/g}$)	Th ($\mu\text{g/g}$)	Th/U	$^{208}\text{Pb}/^{206}\text{Pb}$	1 σ	$^{207}\text{Pb}/^{206}\text{Pb}$	1 σ	$^{208}\text{Pb}/^{232}\text{Th}$	1 σ	f208 from 207(%)	207—corr $^{208}\text{Pb}/^{232}\text{Th}$	1 σ	204—corr spot ages		$^{208}\text{Pb}/^{232}\text{Th}$	1 σ (abs.)	207—corr $^{208}\text{Pb}/^{232}\text{Th}$	1 σ (abs.)	207—corr age (Ma)	207—corr age (Ma)		
														$^{208}\text{Pb}/^{232}\text{Th}$	1 σ	$^{208}\text{Pb}/^{232}\text{Th}$	1 σ	$^{208}\text{Pb}/^{232}\text{Th}$	1 σ				
B	BALZ2@26	110	6800	62	5432	95	0.061	16.1	0.001472	1.6	0.2	0.001461	1.8	29.51	0.52	0.001468	1.6	29.65	0.48				
	BALZ2@27	88	6500	74	/	0	0.165	10.7	0.001500	1.8	1.3	0.001500	/	30.29	/	0.001480	1.8	29.90	0.54				
	BALZ2@28	63	5800	92	109	11	0.715	2.7	0.002091	1.1	28.7	0.001347	4.1	27.22	1.11	0.001492	1.4	30.13	0.41				
	BALZ2@29	20	2100	104	1859	95	0.235	150	0.001517	1.4	2.4	0.001485	2.4	30.00	0.72	0.001481	1.4	29.91	0.43				
	BALZ2@30	14	1700	120	/	0	0.150	27.7	0.001558	1.1	1.0	0.001558	/	31.47	/	0.001542	1.1	31.15	0.35				
	BALZ2@46	41	5900	142	3122	67	0.069	14.8	0.001471	1.5	0.3	0.001453	1.7	29.34	0.50	0.001467	1.5	29.63	0.44				
	BALZ2@47	35	3200	90	685	47	0.121	20.0	0.001480	1.2	0.6	0.001396	2.9	28.21	0.82	0.001471	1.2	29.71	0.37				
	BALZ2@48	67	3600	54	/	0	0.163	19.1	0.001561	1.0	1.1	0.001621	2.2	32.74	0.70	0.001545	1.1	31.20	0.34				
	BALZ2@49	71	3800	54	/	0	0.117	16.5	0.001495	1.6	1.2	0.001495	/	30.20	/	0.001478	1.6	29.85	0.47				
	BALZ2@50	98	5500	56	/	0	0.106	17.3	0.001553	1.5	0.9	0.001553	/	31.37	/	0.001539	1.5	31.09	0.46				
C	BALZ2@01	96	7100	74	175	8	0.529	1.7	0.001551	3.1	20.3	0.001209	3.0	24.43	0.74	0.001237	3.2	24.99	0.79				
	BALZ2@02	82	5500	67	151	10	0.519	2.6	0.001445	3.2	16.7	0.001076	3.6	21.73	0.78	0.001203	3.3	24.29	0.79				
	BALZ2@12	130	8600	66	437	16	0.459	3.2	0.001440	2.9	9.0	0.001313	3.0	26.52	0.80	0.001310	2.9	26.47	0.77				
	BALZ2@24	25	2500	100	139	20	0.678	4.8	0.001788	1.1	21.9	0.001290	5.7	26.05	1.48	0.001396	1.5	28.20	0.44				
	BALZ2@25	86	5600	65	/	0	0.077	16.8	0.001349	1.1	0.4	0.001349	/	27.24	/	0.001343	1.1	27.13	0.31				
	BALZ2@13	67	4100	61	103	8	0.651	1.9	0.001915	3.1	32.7	0.001196	3.7	24.16	0.89	0.001288	3.1	26.02	0.82				
	BALZ2@15	82	3500	43	152	16	0.578	3.0	0.001710	2.6	28.2	0.001275	4.4	25.75	1.13	0.001228	2.8	24.81	0.68				
	BALZ2@16	130	3600	28	151	16	0.459	3.3	0.001576	2.6	22.4	0.001173	4.5	23.70	1.06	0.001224	2.8	24.73	0.68				
	BALZ2@17	140	3800	27	273	20	0.421	3.5	0.001506	2.6	16.4	0.001293	3.6	26.11	0.93	0.001259	2.7	25.43	0.68				
	BALZ2@19	85	3100	36	175	12	0.380	2.8	0.001464	3.3	15.2	0.001152	3.8	23.26	0.88	0.001241	3.3	25.07	0.83				
D	BALZ2@21	200	3500	18	237	20	0.361	3.9	0.001501	2.7	15.5	0.001257	4.0	25.38	1.01	0.001268	2.7	25.62	0.70				
	BALZ2@22	250	4200	17	197	19	0.391	3.8	0.001567	2.7	16.8	0.001283	4.3	25.92	1.12	0.001304	2.8	26.34	0.74				
	BALZ2@14	45	3100	68	98	14	0.573	3.2	0.001555	2.7	31.2	0.000944	5.6	19.07	1.07	0.001070	2.9	21.61	0.63				
D	BALZ2@23	210	3200	15	86	11	0.628	2.2	0.002683	2.6	45.8	0.001504	5.1	30.37	1.54	0.001455	3.1	29.39	0.90				
	BALZ2@20	170	3500	21	83	17	0.279	4.8	0.000688	2.6	20.4	0.000368	8.2	7.43	0.61	0.000548	2.8	11.08	0.31				
D	BALZ2@51	42	2800	67	62	18	0.678	4.1	0.001293	3.2	57.2	0.000542	11.8	10.96	1.29	0.000553	5.6	11.18	0.63				

Table 3 (continued)

Groups	Analysis ID	Th ($\mu\text{g/g}$)	U ($\mu\text{g/g}$)	Th/U	$^{208}\text{Pb}/^{206}\text{Pb}$	1 σ	$^{207}\text{Pb}/^{206}\text{Pb}$	1 σ	$^{208}\text{Pb}/^{232}\text{Th}$	1 σ	f208 from 207(%)	204—corr $^{208}\text{Pb}/^{232}\text{Th}$	1 σ	204—corr spot ages		207—corr		207—corr spot ages	
														$^{208}\text{Pb}/^{232}\text{Th}$	1 σ	$^{208}\text{Pb}/^{232}\text{Th}$	1 σ	$^{208}\text{Pb}/^{232}\text{Th}$	1 σ
<i>Argentera Massif</i>																			
A	MORI@006	9	4800	551	712	19	0.473	5.3	0.000786	2.0	2.6	0.000743	2.2	15.02	0.32	0.000766	2.0	15.47	0.31
	MORI@007	9	3500	369	555	19	0.476	5.5	0.000805	2.3	3.3	0.000749	2.6	15.13	0.39	0.000779	2.3	15.73	0.37
	MORI@008	10	2400	238	426	21	0.391	5.8	0.000803	2.1	4.2	0.000737	2.7	14.90	0.40	0.000770	2.1	15.55	0.33
	MORI@009	4	3000	742	792	26	0.446	5.5	0.000820	2.6	4.3	0.000786	2.8	15.88	0.44	0.000785	2.6	15.86	0.41
	MORI@10	6	3700	598	609	22	0.503	4.9	0.000795	2.1	4.8	0.000744	2.4	15.04	0.36	0.000756	2.1	15.28	0.32
	MORI@11	10	3500	345	450	19	0.449	5.4	0.000803	2.1	3.9	0.000734	2.5	14.82	0.37	0.000772	2.1	15.59	0.33
	MORI@12	10	5000	500	541	18	0.446	5.3	0.000786	2.2	3.0	0.000730	2.4	14.74	0.36	0.000762	2.2	15.40	0.34
	MORI@13	10	4600	484	1097	27	0.366	6.2	0.000782	2.0	2.4	0.000754	2.2	15.23	0.33	0.000763	2.0	15.41	0.31
	MORI@14	8	3400	422	866	22	0.364	5.7	0.000731	2.2	2.3	0.000698	2.3	14.10	0.33	0.000714	2.2	14.43	0.32
	MORI@15	14	3400	252	440	19	0.532	4.7	0.000805	2.1	6.1	0.000734	2.6	14.83	0.38	0.000756	2.1	15.27	0.33
	MORI@16	13	2800	212	443	21	0.425	5.4	0.000780	2.2	4.9	0.000712	2.7	14.40	0.39	0.000742	2.2	14.99	0.33
	MORI@17	14	2700	195	591	25	0.451	5.4	0.000785	2.2	5.4	0.000734	2.7	14.83	0.40	0.000742	2.3	15.00	0.34
	MORI@18	14	2400	167	609	15	0.270	5.5	0.000715	1.9	1.5	0.000672	2.1	13.58	0.28	0.000704	1.9	14.23	0.28
B	MORI@001	54	2500	47	434	21	0.211	4.2	0.000810	2.1	5.9	0.000738	2.7	14.91	0.40	0.000762	2.2	15.39	0.33
	MORI@002	51	3300	65	637	21	0.205	4.4	0.000772	2.0	3.7	0.000726	2.3	14.66	0.33	0.000744	2.0	15.03	0.30
	MORI@003	38	3700	97	453	17	0.202	4.5	0.000737	2.3	3.1	0.000674	2.5	13.62	0.34	0.000714	2.3	14.42	0.33
	MORI@004	51	4400	86	555	17	0.222	4.2	0.000777	2.1	3.1	0.000723	2.3	14.61	0.33	0.000753	2.1	15.21	0.32
	MORI@005	49	4400	90	843	20	0.188	4.6	0.000767	2.0	2.3	0.000735	2.1	14.85	0.32	0.000749	2.0	15.14	0.30
	MORI@20	55	1900	35	586	15	0.134	3.7	0.000799	2.1	2.5	0.000746	2.2	15.07	0.33	0.000779	2.1	15.74	0.33
	MORI@21	55	1600	29	548	16	0.186	3.4	0.000804	2.1	4.0	0.000747	2.3	15.10	0.34	0.000772	2.1	15.59	0.33
	MORI@22	71	1700	24	840	21	0.164	3.8	0.000777	2.0	3.5	0.000742	2.1	14.98	0.31	0.000750	2.0	15.15	0.30
	MORI@23	54	1200	22	463	18	0.160	4.0	0.000734	2.0	4.0	0.000672	2.4	13.59	0.32	0.000704	2.0	14.22	0.29
	VINA@17	32	29,000	904	1855	11	0.240	4.4	0.000821	1.5	0.4	0.000804	1.5	16.25	0.25	0.000818	1.5	16.53	0.25
	VINA@20	15	12,000	777	564	10	0.685	2.5	0.000837	1.5	5.1	0.000780	1.6	15.76	0.25	0.000795	1.5	16.06	0.25
	VINA@22	29	20,000	699	667	8	0.615	2.0	0.000861	1.5	4.0	0.000811	1.5	16.39	0.25	0.000826	1.5	16.70	0.26
	VINA@23	21	11,000	528	685	14	0.556	3.8	0.000817	1.7	2.9	0.000771	1.7	15.58	0.27	0.000793	1.7	16.02	0.27
	VINA@24	28	20,000	706	1423	13	0.251	5.2	0.000822	1.6	0.5	0.000800	1.6	16.16	0.26	0.000818	1.6	16.52	0.27
	VINA@25	34	20,000	595	2366	17	0.240	5.1	0.000819	1.6	0.5	0.000806	1.6	16.28	0.25	0.000815	1.6	16.46	0.26
	VINA@26	35	23,000	665	307	5	0.676	1.5	0.000871	1.6	7.4	0.000761	1.6	15.38	0.24	0.000807	1.6	16.30	0.26
	VINA@18	31	37,000	1185	1499	9	0.359	3.6	0.000743	1.5	0.5	0.000724	1.5	14.62	0.22	0.000739	1.5	14.93	0.23

Table 3 (continued)

Groups	Analysis ID	U ($\mu\text{g/g}$)	Th ($\mu\text{g/g}$)	Th/U	$^{208}\text{Pb}/^{204}\text{Pb}$	1σ	$^{207}\text{Pb}/^{206}\text{Pb}$	1σ	$^{208}\text{Pb}/^{232}\text{Th}$	1σ	f208 from 207(%)	$^{208}\text{Pb}/^{232}\text{Th}$	1σ	204—corr spot ages		207—corr		207—corr spot ages		207—corr	
														$^{208}\text{Pb}/^{232}\text{Th}$	1σ	$^{208}\text{Pb}/^{232}\text{Th}$	1σ	$^{208}\text{Pb}/^{232}\text{Th}$	1σ	$^{208}\text{Pb}/^{232}\text{Th}$	1σ
B	VINA@19	100	32,000	320	1019	8	0.383	2.5	0.000655	1.6	1.5	0.000631	1.6	12.74	0.20	0.000646	1.6	13.04	0.21		
	VINA@21	24	19,000	786	760	11	0.594	2.9	0.000744	1.5	3.0	0.000706	1.6	14.26	0.22	0.000722	1.5	14.58	0.23		
	VINA@06	28	8200	290	1538	19	0.190	6.0	0.000788	1.6	0.7	0.000768	1.7	15.51	0.26	0.000782	1.6	15.81	0.26		
	VINA@07	28	83,000	295	1741	20	0.209	5.9	0.000775	1.6	0.7	0.000758	1.6	15.31	0.25	0.000769	1.6	15.55	0.25		
	VINA@08	22	71,000	326	1211	19	0.203	6.4	0.000732	1.6	0.8	0.000709	1.7	14.32	0.24	0.000727	1.6	14.68	0.24		
	VINA@09	29	68,000	235	1132	19	0.209	6.4	0.000754	1.6	0.8	0.000728	1.6	14.72	0.24	0.000748	1.6	15.12	0.24		
C1	VINA@10	29	73,000	252	1192	19	0.194	6.7	0.000748	1.6	0.7	0.000724	1.6	14.63	0.24	0.000743	1.6	15.01	0.24		
	VINA@11	23	28,000	121	346	15	0.508	3.3	0.000879	1.8	9.9	0.000781	2.3	15.78	0.37	0.000792	1.8	16.01	0.29		
	VINA@12	29	19,000	65	816	30	0.130	7.5	0.000746	1.8	1.6	0.000725	2.4	14.64	0.35	0.000734	1.8	14.83	0.27		
	VINA@13	23	18,000	79	903	33	0.132	8.2	0.000740	2.3	1.6	0.000708	2.6	14.30	0.37	0.000728	2.3	14.71	0.33		
	VINA@14	21	25,000	119	1008	28	0.122	9.1	0.000778	2.0	0.8	0.000749	2.2	15.12	0.33	0.000772	2.0	15.60	0.31		
	VINA@15	14	24,000	169	590	23	0.274	5.3	0.000805	1.9	3.8	0.000752	2.4	15.20	0.36	0.000775	1.9	15.65	0.30		
C2	VINA@16	19	27,000	144	1390	33	0.164	7.9	0.000784	1.8	1.2	0.000762	2.0	15.40	0.30	0.000775	1.8	15.65	0.28		
	VINA@01	28	42,000	150	1189	24	0.113	8.0	0.000751	1.6	0.6	0.000727	1.8	14.69	0.26	0.000747	1.6	15.09	0.25		
	VINA@02	33	41,000	124	1905	31	0.116	8.4	0.000708	1.7	0.6	0.000697	1.8	14.09	0.25	0.000704	1.7	14.23	0.24		
	VINA@03	27	37,000	139	1344	28	0.140	8.3	0.000716	1.7	0.8	0.000696	1.9	14.06	0.27	0.000711	1.8	14.36	0.25		
	VINA@04	15	39,000	258	1327	27	0.160	7.9	0.000714	1.9	0.9	0.000697	2.0	14.07	0.28	0.000708	1.9	14.30	0.27		
	VINA@05	30	36,000	119	1168	27	0.136	8.4	0.000706	1.8	0.8	0.000682	1.9	13.79	0.27	0.000700	1.8	14.14	0.25		
A	GESS@25	47	7200	152	557	12	0.305	3.3	0.000796	2.0	3.2	0.000741	2.1	14.97	0.31	0.000771	2.0	15.57	0.32		
	GESS@26	17	1500	88	130	13	0.591	2.5	0.001153	2.3	30.3	0.000810	4.1	16.36	0.66	0.000803	2.6	16.23	0.41		
	GESS@27	19	4900	256	481	16	0.398	4.0	0.000797	2.1	4.4	0.000733	2.3	14.81	0.34	0.000762	2.1	15.39	0.33		
	GESS@24	23	1200	51	145	16	0.439	3.6	0.000746	2.3	19.1	0.000547	4.6	11.06	0.50	0.000603	2.5	12.19	0.30		

Table 3 (continued)

Groups	Analysis ID	U ($\mu\text{g/g}$)	Th ($\mu\text{g/g}$)	Th/U	$^{208}\text{Pb}/^{204}\text{Pb}$ (%)	$^{207}\text{Pb}/^{204}\text{Pb}$ (%)	$^{208}\text{Pb}/^{232}\text{Th}$ 1 σ	$^{208}\text{Pb}/^{232}\text{Th}$ 1 σ from 207(%)	f_{208}	204—corr spot ages			207—corr			207—corr spot ages			
										$^{208}\text{Pb}/^{232}\text{Th}$ 1 σ	$^{208}\text{Pb}/^{232}\text{Th}$ 1 σ Age (Ma)	$^{208}\text{Pb}/^{232}\text{Th}$ 1 σ (abs.)	$^{208}\text{Pb}/^{232}\text{Th}$ 1 σ	$^{208}\text{Pb}/^{232}\text{Th}$ 1 σ (%)	$^{208}\text{Pb}/^{232}\text{Th}$ 1 σ Age (Ma)	$^{208}\text{Pb}/^{232}\text{Th}$ 1 σ (%)	$^{208}\text{Pb}/^{232}\text{Th}$ 1 σ Age (Ma)		
B	GESS1@01	28	2300	83	599	33	0.162	7.5	0.000769	2.2	3.2	0.000720	3.0	14.54	0.43	0.000745	2.2	15.05	0.33
	GESS1@02	86	3600	42	531	32	0.209	6.7	0.000805	2.5	4.4	0.000759	3.4	15.33	0.52	0.000769	2.5	15.53	0.39
	GESS1@03	160	7800	49	798	30	0.126	7.5	0.000721	2.0	1.7	0.000686	2.4	13.86	0.34	0.000709	2.1	14.32	0.29
	GESS1@06	17	1200	69	428	22	0.224	5.9	0.000751	2.7	3.5	0.000683	3.2	13.80	0.44	0.000724	2.7	14.63	0.40
	GESS1@10	21	3800	185	633	13	0.437	3.1	0.000811	1.9	4.0	0.000761	2.0	15.38	0.31	0.000778	1.9	15.77	0.31
	GESS1@11	23	3300	141	922	17	0.162	6.0	0.000708	1.9	0.9	0.000679	2.0	13.71	0.27	0.000702	1.9	14.19	0.28
	GESS1@12	23	3300	142	1520	22	0.235	5.3	0.000726	1.9	1.3	0.000707	2.0	14.29	0.28	0.000716	1.9	14.47	0.28
	GESS1@15	50	1400	28	535	20	0.112	4.7	0.000769	2.2	2.4	0.000714	2.5	14.42	0.36	0.000751	2.2	15.17	0.33
	GESS1@16	52	1200	23	1089	28	0.093	5.1	0.000768	2.2	1.8	0.000741	2.3	14.98	0.35	0.000754	2.2	15.24	0.33
	GESS1@17	55	1500	27	755	24	0.104	4.9	0.000774	2.0	2.1	0.000735	2.3	14.85	0.34	0.000758	2.0	15.31	0.31
	GESS1@18	42	1100	26	1062	36	0.104	6.3	0.000748	2.2	2.2	0.000721	2.5	14.56	0.36	0.000732	2.2	14.78	0.33
	GESS1@19	43	3200	75	225	9	0.531	1.9	0.000884	2.0	14.9	0.000732	2.2	14.79	0.33	0.000752	2.0	15.20	0.30
	GESS1@20	61	2400	39	355	13	0.316	2.7	0.000806	2.1	8.3	0.000718	2.4	14.52	0.35	0.000739	2.2	14.94	0.32
	GESS1@23	59	2100	36	161	10	0.418	2.2	0.000885	2.8	17.2	0.000673	3.1	13.60	0.42	0.000732	2.8	14.80	0.41
	GESS1@05	19	890	47	415	25	0.137	7.4	0.000689	2.4	2.5	0.000625	3.2	12.63	0.41	0.000671	2.4	13.56	0.33
	GESS1@08	26	1200	45	982	31	0.178	6.9	0.000671	2.1	2.1	0.000644	2.4	13.02	0.31	0.000656	2.1	13.26	0.28
	GESS1@09	25	1500	59	954	27	0.166	6.7	0.000697	2.4	1.7	0.000669	2.6	13.51	0.35	0.000685	2.4	13.84	0.33
	GESS1@21	74	2300	31	1030	23	0.099	5.7	0.000684	2.0	1.1	0.000658	2.1	13.30	0.28	0.000676	2.0	13.66	0.28
	GESS1@22	59	1200	21	319	19	0.215	4.5	0.000729	2.3	6.3	0.000640	3.1	12.94	0.40	0.000682	2.3	13.78	0.32
	GESS1@04	180	7700	43	884	36	0.116	7.8	0.000618	2.2	2.1	0.000591	2.6	11.94	0.31	0.000605	2.2	12.23	0.27
	GESS1@07	23	700	30	609	32	0.160	7.4	0.000614	2.4	2.9	0.000584	3.1	11.80	0.36	0.000596	2.4	12.05	0.29
	GESS1@13	31	3900	127	1425	22	0.190	6.5	0.000641	1.9	0.9	0.000624	2.0	12.60	0.25	0.000636	1.9	12.84	0.25
	GESS1@14	26	2700	105	2697	47	0.144	10.0	0.000637	2.1	0.8	0.000628	2.2	12.68	0.28	0.000632	2.1	12.77	0.27

Table 4 Summary of fissure monazite growth domains weighted mean ages and spot age ranges

Sample domain	Figure	Zoning of the grains	Weighted mean domain $^{208}\text{Pb}/^{232}\text{Th}$ ages (Ma, $\pm 1\sigma$)	MSWD	Number of analyses	Spot $^{208}\text{Pb}/^{232}\text{Th}$ age range of entire grain (Ma, $\pm 1\sigma$)
VIU1—B	3a	Regular	29.9 \pm 0.5	3.7	14	33.2 \pm 0.5—28.5 \pm 0.5
BALZI2—A	3b	Patchy border	36.0 \pm 0.6	0.79	5	50.1 \pm 0.6—11.2 \pm 0.6
BALZI2—B			30.3 \pm 0.5	2.80	10	
BALZI2—C			25.4 \pm 0.5	0.69	7	
MORI1—A	3c	Regular	15.2 \pm 0.3	2.3	13	15.9 \pm 0.4—14.2 \pm 0.3
MORI1—B			15.1 \pm 0.4	2.6	9	
VINA1—A	3d	Regular	16.4 \pm 0.2	0.97	7	16.7 \pm 0.3—13.0 \pm 0.2
VINA1—B			15.2 \pm 0.6	3.3	5	
VINA1—C1			15.4 \pm 0.5	3.0	6	
VINA1—C2			14.4 \pm 0.5	2.4	5	
GESSION1—B	3e	Patchy border	14.9 \pm 0.3	2.2	14	16.2 \pm 0.4—12.1 \pm 0.3

greenschist facies) and sample BALZI2 from the Briançonnais Zone (blueschist/greenschist facies). Samples MORI1, VINA1 and GESSION1 were collected in the Argentera Massif (greenschist facies) (Table 1; Fig. 1). All the dated grains come from vertical fissures hosted by gneiss, except BALZI2 sample for which information on fissure orientation is missing (metarhyolite block in scree; Table 1).

Field images showing fissures in high-pressure overprinted regions are displayed in Fig. 2b–f, between the Saas Fee locality in the north and the Costa Balzi Rossi locality in the south (Fig. 1). Alpine fissures from these regions are all oriented subvertically with a strike ranging between N145–180 (Fig. 2a), as seen in Fig. 2b–e. The Costa Balzi Rossi area (Fig. 2f) is a famous locality for REE minerals (Bracco et al. 2012). As the analysed monazite was found in a block in scree (R. Bracco, pers. comm.), the original orientation of the fissure is not known. Samples VIU1 and BALZI2 were collected in the Valle di Viù (Fig. 2d) and Costa Balzi Rossi (Fig. 2f) localities, respectively.

In the Argentera Massif, Alpine fissures are also oriented vertically (Fig. 2g–h) with a strike in the range between N005–N020 (Fig. 2a). Samples MORI1 and VINA1 were collected in the Stura Valley near the Sambouco locality and GESSION1 grain further south, in the Gesso Valley (Fig. 1; Table 1).

4.2 Fissure monazite dating

In this section, chemical, textural and chronological data are presented in detail for each grain. Figure 3 gives information on Th–U content obtained by ion probe (left) and on chemical domains distinguishable on BSE images (centre). These combined data were used to define mineral growth domains, allowing calculation of weighted

mean $^{208}\text{Pb}-^{232}\text{Th}$ ages (right) for growth domains. Ion probe and LA-ICP-MS spot locations are indicated on BSE images as solid and dashed circles, respectively.

4.2.1 Grains from high-pressure regions

VIU1 is a ~700 μm -long grain (Fig. 3a) composed of two major chemical domains. Domain A comprises the bright bottom part in BSE image with Th/U ratio close to 100. Domain B, comprising the major part of the grain, is characterised by a darker colour in BSE image, related to lower Th and U contents of ~12,000–22,200 and 240–260 $\mu\text{g/g}$ respectively (Table 3). A weighted mean age of 29.9 ± 0.5 Ma (MSWD = 3.7, n = 14) is calculated for domain B (Table 4).

BALZI2 (Fig. 3b) is a complex grain that underwent several alteration episodes as indicated by the presence of dissolution trails (red-dashed lines on Fig. 3b) and pores (indicated by red arrows on Fig. 3b) visible on the BSE image. The oldest part of the mineral is mainly preserved in the lower-right part of the grain (BALZI2-A domain): it yields a distinct Th/U ratio of between 6 and 50 and providing a weighted mean age of 36.0 ± 0.6 Ma (MSWD = 0.79, n = 5; Table 4). Spots 34 to 40 of BALZI2-A domain display older and scattered dates, which may indicate a complex early history of the grain. Most analyses located in the rim and in the upper part of the grain, BALZI2-B, C and D domains, display Th/U ratios ranging between 20 and 140 overlapping with domain A chemistry (Table 3). BALZI2-B and C domains are chemically comparable, but provide distinct weighted mean ages of 30.3 ± 0.5 Ma (MSWD = 2.80, n = 10) and 25.4 ± 0.5 Ma (MSWD = 0.69, n = 10; Table 4). A few analyses (spot 1, 2, 12, 14, 23, 24, 25 and 31, open symbols) sit on or close to dissolution trails and give younger ages (Table 3). These analyses are excluded from weighted mean age

Table 5 LA-ICP-MS analyses of element concentrations in monazite domains ($\mu\text{g/g}$). Note that Yb and Lu correspond to maximum concentrations because of potential GdO and TbO interferences during measurement

Sample domain/ Element (isotope)	VIU1—A	VIU1—B	VIU1—C	BALZ12—C	BALZ12—B	MORI1—B	MORI1—A	MORI1—A
spot #	7,8,9	10,11,12	13,14,15,16	68,69,70	71,72,73	74,75,76,77	36,37,38,39	40,41,42
B11	<0.24	<1	<0.34	<0.57	<0.4	<0.52	0.4±0.1	1±0.1
Nd23	<0.16	<0.7	<0.19	<0.22	6±4	<0.25	0.8±0.9	5±3
S129	<149	<1290	<341	<580	<380	<390	<233	<207
P31	109,100±1700	103,900±800	106,500±200	107,700±1800	107,500±200	106,000±800	111,600±1800	111,900±1200
Ca43	4060±390	3460±230	3090±610	4020±550	1360±110	890±460	3780±170	4230±100
Ti49	<0.47	<3	0.7±0.1	<0.37	<0.91	<1	<0.41	<0.31
As75	296±11	252±4	296±13	363±29	367±2	376±27	349±3	347±6
Sr88	630±58	677±39	485±136	1540±170	473±12	382±206	871±32	949±22
Y89	4150±430	3090±70	5000±500	7800±2100	7700±400	3500±260	11,020±170	9630±430
Mo95	0.8±0.03	<0.42	0.8±0.2	0.7±0.1	0.7±0.1	0.9±0.3	1±0.2	0.9±0.1
Ba137	0.3±0.1	<1	0.4±0.1	0.4±0.1	0.7±0.5	0.3±0.1	0.5±0.1	1±0.2
La139	114,500±5700	139,600±900	121,200±7800	154,300±18,400	141,500±2000	144,800±2600	119,750±640	120,700±1100
Ce140	298,400±2200	319,260±540	301,200±4000	289,900±7400	294,800±1600	307,100±1400	272,400±1700	275,100±2400
Pr141	29,150±610	28,170±110	29,310±490	31,000±1200	32,500±80	33,110±190	32,910±220	33,000±180
Nd146	119,300±4100	105,320±640	119,900±5500	115,300±10,800	123,300±1200	121,900±1800	133,000±1200	132,740±270
Sm147	22,600±810	18,300±160	23,600±2000	18,900±3600	19,470±657	17,140±340	27,920±170	27,460±490
Eu151	4400±100	3430±12	4780±410	2270±470	2500±60	1630±120	2230±20	2090±60
Gd157	15,780±310	11,310±30	17,130±1650	10,910±2270	11,980±400	9720±590	19,430±250	18,830±570
Tb159	1300±10	887±8	1510±190	1040±240	1120±50	783±55	1720±30	1650±50
Dy163	3560±240	2300±30	4120±510	3890±990	4020±180	2350±210	5450±60	5280±170
Ho165	234±22	154±3	282±32	394±111	395±19	194±21	494±12	445±22
Er167	189±22	134±6	245±23	567±159	531±26	219±26	559±11	475±25
Tm169	7±1	5±0.2	10±1	37±9	31±2	11±1	28±1	23±1
Yb173	15±2	10.6±0.1	22±2	119±26	90±5	29±4	66±2	53±3
Lu175	0.7±0.1	0.54±0.05	1.1±0.1	7±1	5.2±0.2	1.5±0.2	3.1±0.1	2.5±0.2
W182	0.14±0.01	0.19±0.04	0.14±0.03	0.2±0.1	0.2±0.1	0.16±0.02	0.17±0.04	0.18±0.03
Th232	23,700±2700	15,400±1500	15,000±2200	2980±1350	3210±490	3670±1040	5420±1070	3570±390
U238	349±97	259±3	234±12	85±55	93±9	48±18	121±5	116±5
							24±1	29±1

Table 5 (continued)

Sample spot #	VINA1—C2	VINA1—B	VINA1—A	VINA1—A	GES1—B	GES1—B	GES1—B
domain / Element (isotope)							
B11	17,18,19,20	21,22,23,24	25,26,27,28	29,30,31,32	33,34,35	50,51,52,53	54,55,56
	<0.34	<0.16	<0.36	<0.54	<0.51	<0.68	<0.53
Nd23	<0.23	<0.12	<0.19	<0.34	<0.48	<0.51	6±7
Si29	<380	<203	<390	<670	1500±250	<810	<840
P31	106,600±1000	109,000±900	106,000±1000	106,300±800	101,900±1800	105,900±1100	107,000±400
Ca43	1140±120	2420±160	3850±120	4840±1010	4700±1100	1860±290	2880±710
Ti49	0.5±0.1	0.4±0.1	0.5±0.1	<1	<1	<0.65	<2
As75	321±8	314±2	303±4	285±17	325±15	363±5	357±8
Sr88	284±18	543±31	861±56	1040±370	1140±220	460±143	655±31
Y89	5400±400	5870±170	5180±80	5440±950	2610±620	8490±790	8600±590
Mo95	0.8±0.1	0.8±0.1	0.8±0.2	0.8±0.2	1.1±0.2	1.0±0.2	0.9±0.3
Ba137	0.32±0.04	0.48±0.04	1±0.1	1±1	1.4±0.6	<0.57	0.8±0.3
La139	140,900±2900	139,800±800	138,780±960	149,100±12,000	129,400±7100	118,500±3100	118,700±1900
Ce140	284,000±2000	285,300±400	282,760±630	287,400±3500	274,500±2970	275,200±4600	273,300±2000
Pr141	33,170±160	32,550±80	32,240±180	31,640±1110	32,750±660	34,450±160	33,930±140
Nd146	129,500±1800	124,400±600	123,000±1200	116,200±6800	129,300±6800	141,500±2100	138,400±1200
Sm147	24,640±610	22,580±230	22,190±330	21,610±1010	26,130±2070	32,470±1230	32,100±1100
Eu151	2070±70	1740±20	1570±20	1430±130	1360±20	2430±220	2230±100
Gd157	16,080±580	13,460±220	14,250±330	12,850±1270	14,170±640	22,430±1340	22,170±1030
Tb159	1260±70	1160±20	1150±20	1050±130	898±86	1850±150	1840±100
Dy163	3410±200	3300±80	3240±70	3010±470	1940±340	5250±470	5230±370
Ho165	255±18	266±7	255±4	241±47	122±28	407±36	398±31
Er167	274±22	310±10	276±10	273±63	104±29	410±43	390±32
Tm169	14±1	17±1	14±1	15±4	4±2	18±2	17±2
Yb173	33±3	45±2	36±2	39±12	10±3	38±6	36±5
Lu175	1.6±0.1	2.3±0.1	1.9±0.2	2±1	0.5±0.2	1.7±0.2	1.7±0.2
W182	0.13±0.03	0.15±0.03	0.14±0.02	0.18±0.03	0.13±0.02	<0.14	0.2±0.1
Th232	3830±210	8040±690	18,200±2100	11,000±2100	37,300±3200	2440±250	5030±770
U238	32±4	33±1	39±2	24±4	57±37	93±7	118±4

The analysed isotopes correspond to the number following each element. Li7, Al27, Mn55, Fe57, In115 and Bi209 were analysed but are below detection. Data entries " $<\text{value}$ " represent measurements below LOD

calculations. Two additional spot analyses (20 and 51, open blue symbols), located in the upper part of the grain, are also sitting on dissolution trails and provide the youngest dates for this grain at around ~ 11 Ma. These youngest dates, labeled BALZI2-D, most likely record the latest phase of monazite alteration.

4.2.2 Monazites from the Argentera Massif

Sample MORI1 (Fig. 3c) displays two distinct Th and U clusters ranging between 1200 and 5000 and 4–70 $\mu\text{g/g}$, respectively labelled as MORI1-A and B domains (Table 3). No clear textural evidence allows distinguishing the different domains without chemical information: but the low and high U contents can be used to distinguish two groups (A = 5–20 $\mu\text{g/g}$ and B = 40–70 $\mu\text{g/g}$). Identical weighted mean ages of 15.2 ± 0.3 (MSWD = 2.3, n = 13) and 15.1 ± 0.4 Ma (MSWD = 2.6, n = 9) were calculated for domains A and B, respectively (Table 4).

The crystal VINA1 (Fig. 3d) is nearly homogeneous in U content (29 $\mu\text{g/g}$ on average), but displays decreasing Th contents from core to rim (Table 3), i.e. from domain A ($\sim 11,200$ – $37,000$ $\mu\text{g/g}$, red symbols), to domain B (~ 1800 – 8400 $\mu\text{g/g}$, orange symbols), to domain C (~ 3600 – 4200 $\mu\text{g/g}$, green and blue symbols), also visible on the BSE image as decreasing brightness. Weighted mean ages of 16.4 ± 0.2 (MSWD = 0.97, n = 7), 15.2 ± 0.6 (MSWD = 3.3, n = 5), 15.4 ± 0.5 Ma (MSWD = 3.0, n = 6) and 14.4 ± 0.5 Ma (MSWD = 2.4, n = 5) were calculated for domains A, B, C1 and C2 (Table 4). Spot analyses 18, 19 and 21 located in domain A (red open symbols), record a younger age that can be explained by the presence of a dissolution trail/pores, probably corresponding to a younger alteration episode.

The grain GESSION1 (Fig. 3e) is composed of a patchy and inclusion-rich core (GESSION1-A domain), characterized by Th/U ratios ranging between 260 and 90 (Table 3), and providing the oldest spot dates of the grain of up

to ~ 16 Ma. One analysis, spot 24 (open red circle), sits on a dissolution trail and give a younger date (Table 3). The second domain (GESSION1-B) constitutes the major part of the crystal and is chemically and isotopically heterogeneous with a Th/U ratio ranging between 20 and 180. A weighted mean age of 14.9 ± 0.3 (MSWD = 2.2, n = 14) is calculated for this second domain (Table 4), but scattered spot ages as young as ~ 12 Ma are also observed (blue open circles in Fig. 3e; Table 4), likely recording a later phase of monazite alteration that has barely affected the chemistry.

4.3 Fissure monazite chemistry

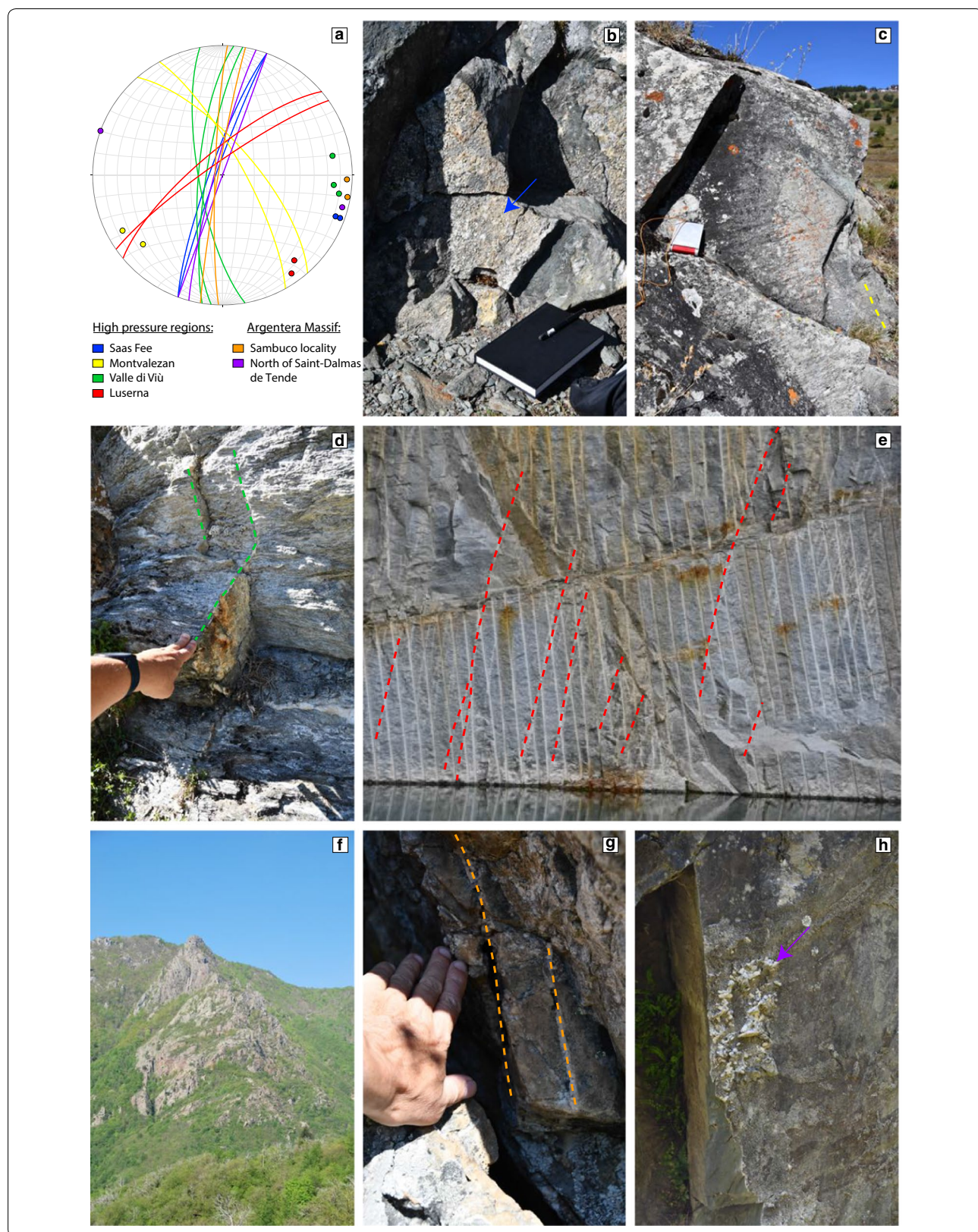
Trace element LA-ICP-MS analyses of dated fissure monazite domains are listed in Table 5. However, due to the larger spot size (24–60 μm) of the LA-ICP-MS, some of the dated domains were too small to be analyzed. Thorium and U contents measured by ion probe and LA-ICP-MS are comparable, which confirms the chemical groups described in Fig. 3.

CI-chondrite-normalised (McDonough and Sun 1995) fissure monazite REE patterns are displayed in Fig. 4. The patterns are generally comparable with some variation in the slope of the HREE: sample VIU1 and GESSION1 having a lower content in HREE than BALZI2, MORI1. There are also minor differences in the negative Eu anomaly ($\text{Eu/Eu}^* = \text{Eu}_N / (\text{Sm}_N \times \text{Gd}_N)^{0.5}$ McLennan 1989): average values of 0.72, 0.46, 0.28, 0.27 and 0.27 for grains VIU1, BALZI2, MORI1, VINA1 and GESSION1. Again, sample VIU1 is distinct with respect to the other grains by a less pronounced Eu anomaly (Fig. 4). Only the MORI1 grain clearly shows different REE patterns in its two age domains (see Additional file 1: Figure S1; Table 5).

Distinct chemical trends of fissure monazites from this study are presented in bivariate plots in Fig. 5a–c. Th and U contents of BALZI2, MORI1 and GESSION1 grains cluster below 10,000 $\mu\text{g/g}$ Th and below 130 $\mu\text{g/g}$ U, whereas

(See figure on next page.)

Fig. 2 **a** Stereographic projection of planes and their poles of subvertical Alpine fissure in the Western Alps. Localities are indicated in Fig. 1. Fissures in high pressure regions and in the Argentera Massif are presented in b-f and g-h, respectively. **b** NNE (N020) striking vertical fissure in amphibolite facies metabasalt of the Zermatt-Saas high-pressure zone. At the locality of Mittaghorn, Saas Fee, Switzerland, the vertical fissure shown contains crystals of albite (pericline), quartz and chlorite (the wall of the fissure is indicated by the blue arrow). **c** Subvertical, SSE (N145) striking fissure in Permo-Carboniferous metaconglomerates at Montvalezan, Savoie, France (yellow-dashed lines), associated with strike-slip faulting (note horizontal lineation). The fissure is located in greenschist-facies overprinted blueschist facies rocks. **d** N (N000) striking, subvertical fissures (green-dashed lines) in greenschist facies overprinted eclogite facies metasedimentary rocks at Margone, Val di Viù, Piedmont, Italy. Sample VIU1 is from this locality. **e** Meta-granitoid rocks at Montoso, Piedmont, exploited as "Pietra di Luserna". The steeply oriented, NE (N050) striking fissures (indicated by red-dashed lines) cutting the horizontal foliation caused bleaching (dissolution of biotite) in the adjacent host rock. Fissure monazite was reported from these quarries (Finello et al. 2007). **f** Permian metarhyolites and metasedimentary rocks forming the mountains of Costa Balzi Rossi, Magliolo, Liguria, Italy. The dated monazite sample BALZI1 derives from fissures located in the wall-forming metarhyolites (Bracco et al. 2012), but was collected in the scree. **g** Vertical N-S (N005) striking fissures (indicated by orange-dashed lines) at the locality Sambuco, Valle Stura, Argentera Massif. Monazite is reported from fissures of this area. Monazites from Vinadio (VINA1) and Moriglione (MORI1) in Valle Stura are from comparable fissures. **h** NNE (N020) striking fissure in metamorphic Permian siltstones of the Argentera Massif, France, ca. 1.5 km north of Saint-Dalmas de Tende, showing milky quartz crystals on fissure wall (violet arrow).



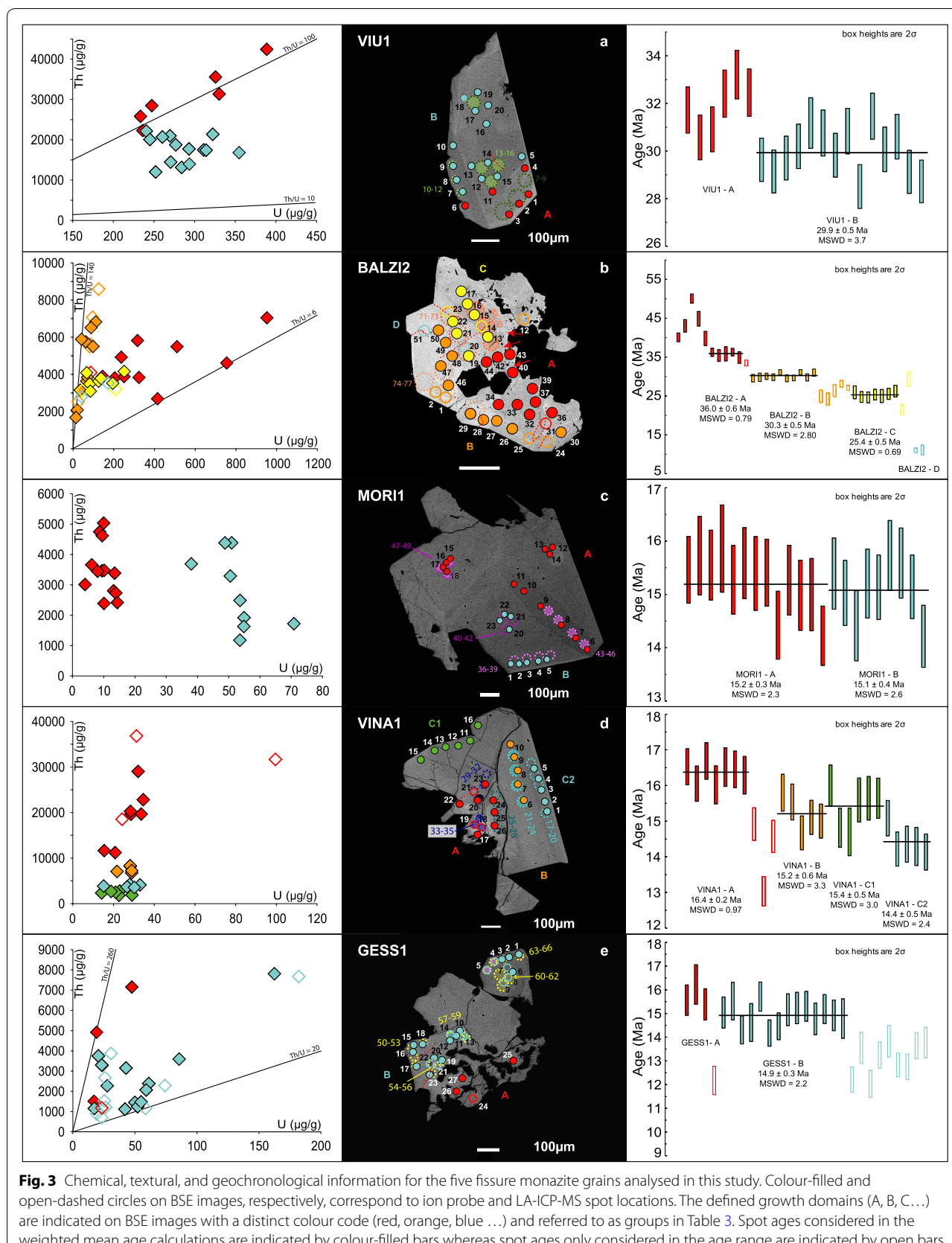
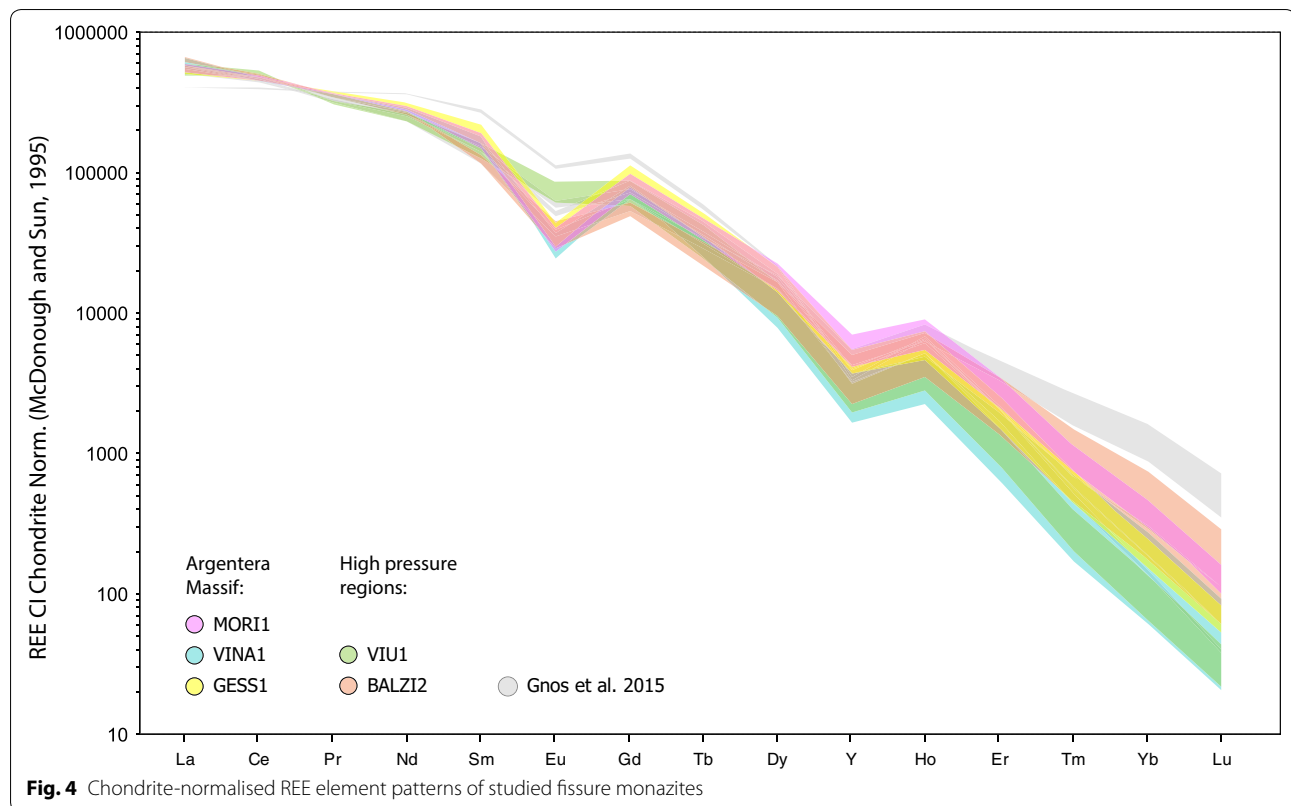


Fig. 3 Chemical, textural, and geochronological information for the five fissure monazite grains analysed in this study. Colour-filled and open-dashed circles on BSE images, respectively, correspond to ion probe and LA-ICP-MS spot locations. The defined growth domains (A, B, C...) are indicated on BSE images with a distinct colour code (red, orange, blue ...) and referred to as groups in Table 3. Spot ages considered in the weighted mean age calculations are indicated by colour-filled bars whereas spot ages only considered in the age range are indicated by open bars (bar length representing the spot age plus its 2 σ uncertainty). Red arrows point to pores indicating dissolution-reprecipitation reactions



VIU1 and VINA1 grains show higher values and distinct average Th/U ratios close to 65 and 500 respectively (Fig. 5a). A positive correlation of Sr and Ca is observed for all the grains (Fig. 5b) whereas Y is correlated negatively with Ce (Fig. 5c).

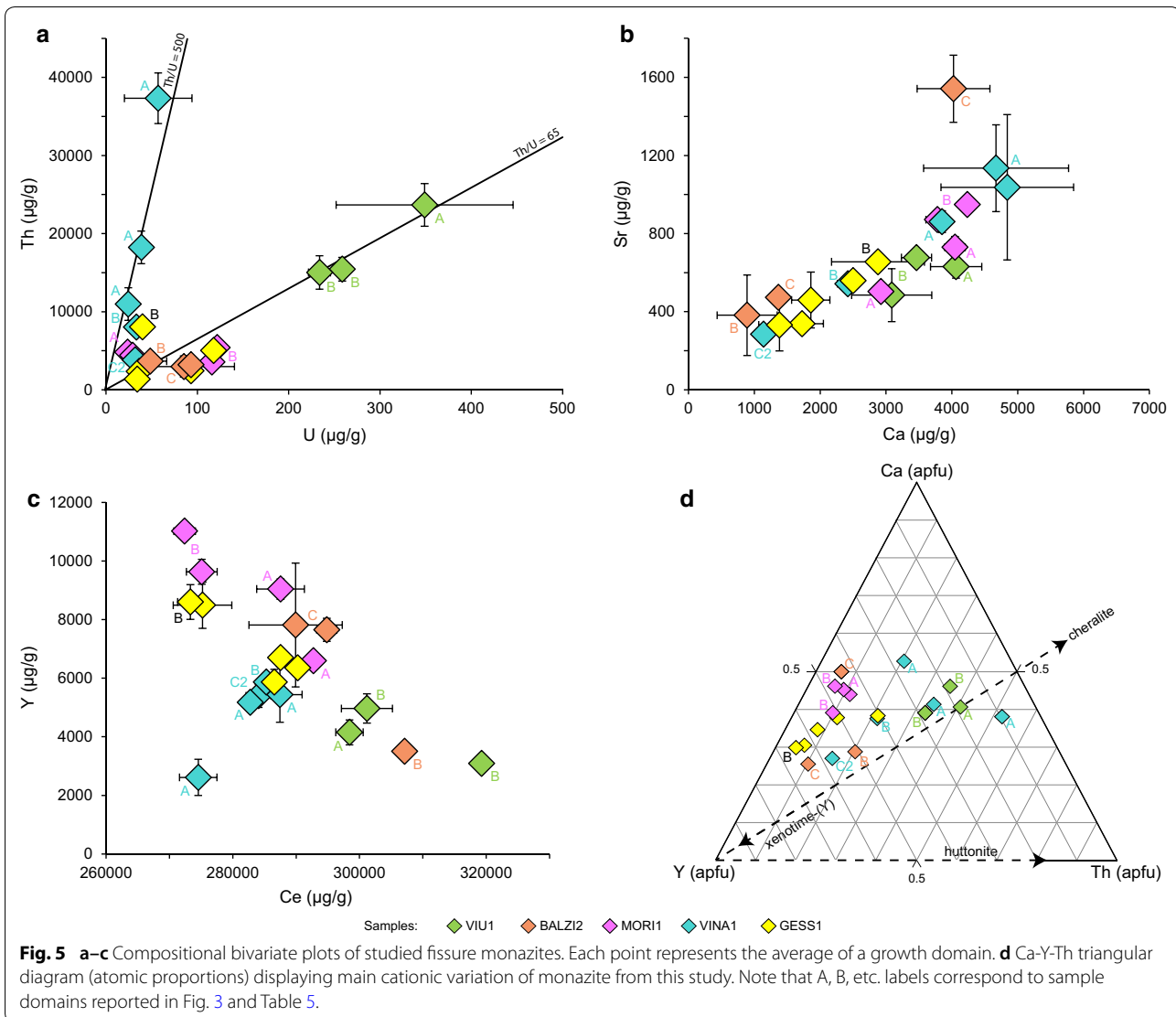
The main chemical variations present in the cationic site of the studied fissure monazites are displayed in a Ca-Y-Th triangular plot (Fig. 5d). Th and Ca increase is related to Y decrease, this corresponds to an increase of the cheralite component, $(\text{Ca}^{2+}, \text{Th}(\text{U})^{4+})(\text{P}^{5+}\text{O}^{2-})_2$, and to a decrease of the xenotime-(Y) component ($\text{Y}^{3+}\text{P}^{5+}\text{O}^{2-}_4$). The lack of Si in the studied monazites (below detection limit of 500 µg/g on average) indicates that the Th pole of the Ca-Y-Th triangular plot corresponding to the huttonite $(\text{Th}(\text{U})^{4+}\text{Si}^{4+}\text{O}^{2-}_4)$ component is very low (Table 5). The Y pole represents the xenotime-(Y) component. The chernovite-(Y), $\text{Y}^{3+}\text{As}^{5+}\text{O}^{2-}_4$ component is negligible due to low As content (average As content: 330 µg/g; Table 5). In summary, VINA1 and VIU1 grains display a higher cheralite component (2 REE³⁺ substituted by Th⁴⁺ and Ca²⁺) whereas the other grains (BALZI2, MORI1 and GEES1) tend to a higher xenotime component (REE³⁺ substituted by Y³⁺) (Fig. 5d). In some cases, REE and trace elements show clear differences between different growth domains, but in many cases differences are too small to distinguish

growth domains. Moreover, our data do not show systematic compositional changes with age (Fig. 5 and Additional file S1). Thus, as described above, growth domains discrimination was essentially based on the combination of textural observations and U-Th contents variation.

5 Discussion

5.1 Fissure monazite crystallization ages

In the Briançonnais Zone, fissure monazite ages record crystallization at ~32 and ~23 Ma (Grand'Homme et al. 2016a) and at ~36, ~30 and 25 Ma in the BALZI2 grain (Figs. 1, 3 and 6). The distinct age domains recorded in BALZI2 capture a crystallization duration of ~11 Ma, possibly up to ~40 Ma if the isolated dates in the core of the grain are considered (Fig. 3; Table 4). Older spot ages around ~45 Ma may indicate that fissure formation occurred already during deformation at high-pressure greenschist facies conditions in this area (Bousquet et al. 2012). The VIU1 monazite grain from the Piemontais Zone records monazite growth mostly at ~30 Ma, possibly with an earlier episode already at ~32 Ma (Figs. 1, 3 and 6; Table 4). Our data thus confirm that fissure formation occurred in the Briançonnais and Piemontais zones mainly in association with the retrograde metamorphic overprinting of the high-pressure rocks during its exhumation, and later in association with strike-slip faulting.

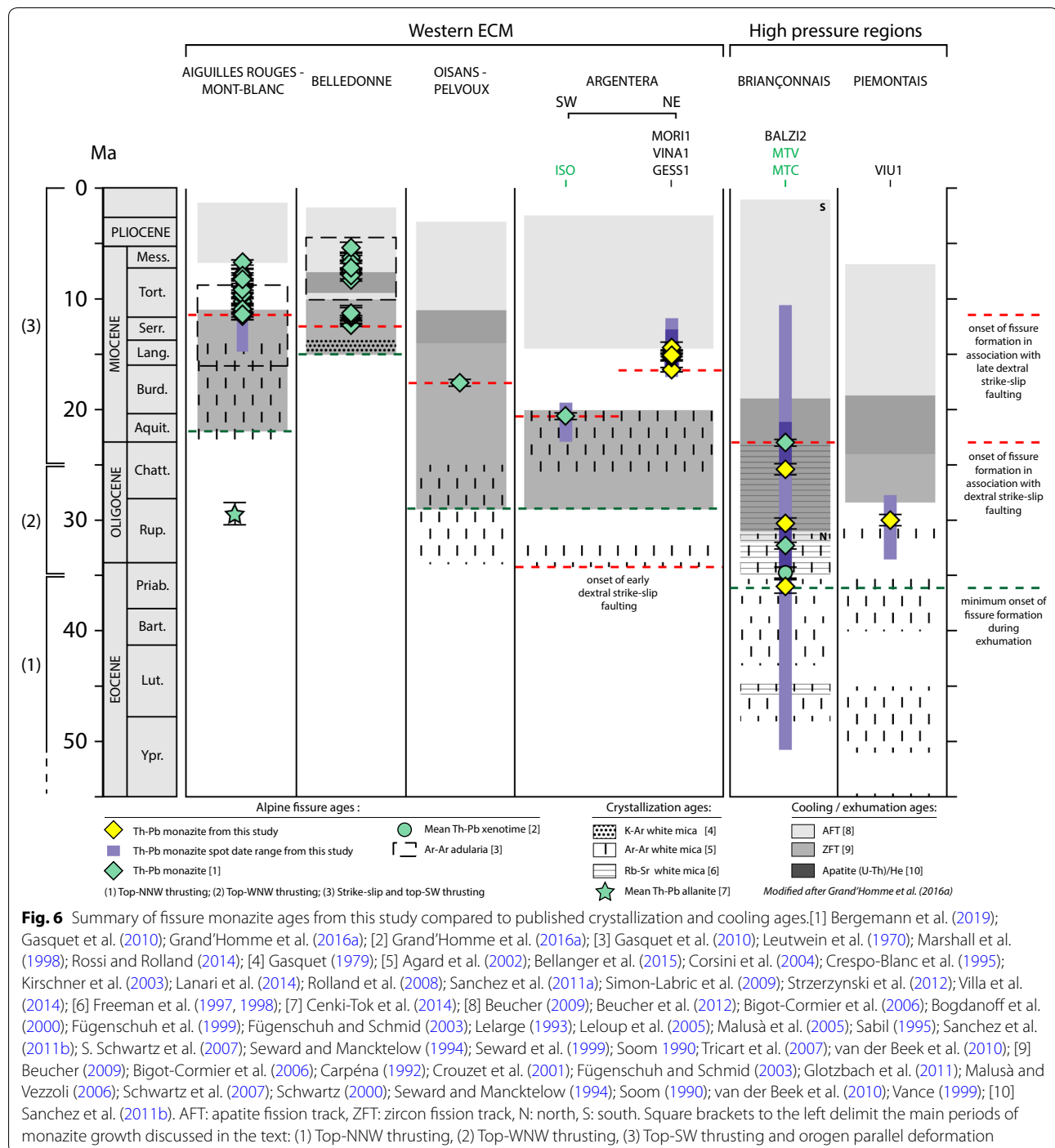


In the ECM of the Western Alps, fissure monazite yield a wide range of ages: (i) ~17.6 Ma for the Pelvoux Massif (Gasquet et al. 2010), (ii) ~20.6 and ~16–14 Ma for the south-western (Grand'Homme et al. 2016a) and north-eastern (MORI1, VINA1 and GESS1 grains) border of the Argentera Massif, (iii) ~12–11 and ~8–5 Ma for the Belledonne Massif (Gasquet et al. 2010; Grand'Homme et al. 2016a) and (iv) ~12–7 Ma for the Aiguilles Rouges and Mont Blanc Massifs (Bergemann et al. 2019; Grand'Homme et al. 2016a; Figs. 1 and 6). However, the ~17.6 Ma fissure monazite from the Pelvoux Massif (Gasquet et al. 2010) is related to the formation of horizontal fissures that formed in association with the development of a steeply oriented foliation, while in the Argentera Massif only vertical fissures developed in association with strike-slip faulting. This shows that the Alpine tectonic evolution of Argentera is different to

all other ECM. Our monazite data indicate that strike-slip faulting ceased in the Argentera Massif at ~14 Ma, whereas dextral strike-slip movements along the western ECM started at ~11–12 Ma (e.g., Steck and Hunziker 1994; Bergemann et al. 2017).

5.2 Comparison with deformation, cooling ages and tectonic evolution of the Western Alps

In order to interpret the newly obtained $^{208}\text{Pb}/^{232}\text{Th}$ monazite crystallization ages (Fig. 6) in a tectonic context, they are compared to available crystallization/deformation and cooling/exhumation ages for the areas of interest, i.e. Argentera Massif, Briançonnais Zone and Piemontais Zone.



5.2.1 Top-NNW thrusting (> 35 Ma)

The oldest fissure monazite age of the Western Alps is recorded at ~36 Ma by BALZI2 grain from the Briançonnais Zone (Figs. 1 and 6) and is interpreted to be related to Late Eocene–earliest Oligocene top-NNW thrusting (episode (1); Table 2) which started at or before 38 Ma (Cardello et al. 2019). This deformation was coeval with

the development of the main foliation during emplacement of the Siviez-Mischabel Nappe dated at 41–36 Ma (Markley et al. 1998). Ar–Ar dating of syn-kinematic phengite from the Modane-Aussois area, west of Ambin (Am on Fig. 1; Strzerynski et al. 2012), suggest that top-NNW thrusting ended at around ~37 Ma during decompression, giving way to WNW-directed thrusting

(episode (2) on Fig. 6; Table 2) from ~ 35 Ma down to at least ~ 32 Ma. A xenotime grain from a fissure located further north in the same high-pressure terrane records an average age of ~ 35 Ma (Grand'Homme et al. 2016a; Fig. 6). According to Freeman et al. (1997), the onset of backthrusting in the Briançonnais is constrained at ~ 34 Ma by Rb–Sr dating of syn-kinematic white mica formed under mid-greenschist facies conditions near the western and northern border of the Grand Paradiso (GP) internal massif (Fig. 6). The fissure monazite domain age constrains the minimal onset of exhumation in the Briançonnais Zone at ~ 36 Ma, but isolated spot ages in BALZI2 point at an even earlier start at ~ 45 Ma. In the Piemontais Zone, greenschist conditions are constrained between ~ 40 and 35 Ma by Ar–Ar dating of phengite (Agard et al. 2002; Fig. 6). Note that fissure monazite and xenotime ages from high-pressure terranes are older than the zircon fission track (ZFT) record, suggesting that these fissure minerals crystallized above a maximum temperature of ~ 380 – 190 °C (e.g. Glotzbach et al. 2010; Ricchi et al. 2019).

5.2.2 Top-WNW thrusting (35–25 Ma)

Slightly younger fissure monazite crystallization ages are recorded in the Briançonnais Zone between ~ 32 and 30 Ma (BALZI2 grain from this study and MTC grain from Grand'Homme et al. 2016a) and in the Piemontais Zone at ~ 30 Ma (VIU1 grain; Figs. 1, 3a, b and 6). These ages correspond to a rapid uplift episode, i.e. exhumation of high-pressure units, that affected the Dora Maira internal massif between ~ 32 and 30 Ma (e.g. Dumont et al. 2012; Rubatto and Hermann, 2003; Schmid et al. 2017). This uplift episode occurred in response to the WNW-directed indentation of the Ivrea mantle wedge (Table 2). Rb–Sr dating of syn-kinematic phengites from Freeman et al. (1997, 1998) show that this second episode of WNW-directed thrusting started at ~ 34 Ma in the eastern part of the Briançonnais Zone (along the NW border of the GP Massif), migrated westward, reaching the current western border of the Briançonnais Zone at ~ 31 Ma (see also Egli et al. 2016), and ended between ~ 27 and 23 Ma (Fig. 6). An $^{40}\text{Ar}/^{39}\text{Ar}$ synkinematic muscovite from the Argentera Massif indicates that dextral strike-slip faulting started at 33.6 ± 0.6 Ma during this period.

5.2.3 Strike slip and top-SW thrusting (25–0 Ma)

The top-WNW-directed thrusting along the PF led to backfolding, backthrusting, and later to the exhumation of the ECM together with westward migration of the deformation front (Table 2). NE-striking dextral strike-slip movements started to develop around and through the internal border of the western ECM. This orogen-parallel deformation episode ((3) on Fig. 6) also coincides

with the development of SW-directed normal faulting along the Simplon Fault and SW-directed thrusting along the Digne Thrust (Hubbard and Mancktelow 1992; Grasemann and Mancktelow 1993).

Fissure monazite crystallization recorded at ~ 23 Ma by Grand'Homme et al. (2016a) related to shear zones activity the Briançonnais Zone Houillère (MTV in Figs. 1 and 2c) occurred during the westward indentation of the Adriatic plate constrained to between 26.8 ± 0.7 Ma and 20.5 ± 0.3 Ma by Ar–Ar dating of syn-kinematic phengite from the Argentera Massif (Sanchez et al. 2011a; Fig. 6) and the onset of the Liguro-Provençal Basin ocean spreading starting during the Aquitanian (e.g. Gattacceca et al. 2007).

The grain BALZI2 records a domain age at ~ 25 Ma (Figs. 1 and 6). We suggest that this monazite domain crystallized at ~ 25 Ma also in association with shear zone activity related to the earliest stages of ocean spreading in the Liguro-Provençal Basin (e.g. Gattacceca et al. 2007; Sanchez et al. 2011a; Schmid et al. 2017).

At the South-Western border of the Argentera Massif, younger monazite crystallization is dated at ~ 20.6 Ma (ISO grain from Grand'Homme et al. 2016a), interpreted to be related to NW-striking dextral shear zones (Grand'Homme et al. 2016a; Fig. 1). This age is in the range of synkinematic phengite of 26.8 ± 0.7 Ma and 20.5 ± 0.3 Ma dated by Sanchez et al. (2011a). This fissure monazite age is contemporaneous with the onset of the anticlockwise rotation of the Corsica-Sardinia block constrained at 20.5 Ma (e.g. Gattacceca et al. 2007; Schmid et al. 2017; stage 3 in Table 2). Most of the Corsica-Sardinia anticlockwise rotation (30°), accommodating the opening of the Liguro-Provençal Basin, occurred between 20.5 and 18 Ma and was active until 16–15 Ma, resulting in a total rotation of 45° (Gattacceca et al. 2007). This age range corresponds almost exactly with the activity of the orogen-parallel stretching related to the Simplon Fault (Grasemann and Mancktelow 1993; Campani et al. 2010). Contemporaneous with this rotational phase, deformation during uplift of the Pelvoux Massif is recorded at ~ 17.6 Ma by a fissure monazite from a horizontal vein (Gasquet et al. 2010). In the north-eastern part of the Argentera Massif, younger fissure monazite ages of 16–14 Ma are interpreted to constrain dextral fault activity related to the end of the Corsica-Sardinia anticlockwise rotation as described by Gattacceca et al. (2007), and mark the onset of (re)-activation of dextral strike-slip faulting along and through the internal border of the western ECM (Figs. 1 and 6).

The middle Miocene dextral strike-slip record movement affecting the western ECM, occurred earlier in the Argentera Massif and shifted then to the other ECMs. Indeed, the fissure monazite ages recording fault activity

along the BSZ or VSZ dextral shear zones in the Argentera Massif (Fig. 1) are between ~16 and 14 Ma (MORI1, VINA1 and GEES1 grains), followed by dextral faulting between ~12 and 11 Ma and between ~8 and 5 Ma in the Belledonne Massif (Gasquet et al. 2010; Grand'Homme, et al. 2016a), and between ~12 and 7 Ma in the Aiguilles Rouges and Mont Blanc massifs (Bergemann et al. 2019; Grand'Homme, et al. 2016a; Figs. 1 and 6). Note that fissures-bearing monazite related to dextral strike-slip movements from the Aiguilles Rouges, Mont-Blanc and Belledonne massifs are sub-vertical and E-W striking (Bergemann et al. 2019; Grand'Homme et al. 2016a). However, NNE-striking vertical fissures are observed between the southern termination of the Argentera Massif and Saint-Dalmas de Tende locality (Fig. 2 h), suggesting that these fissures may have had a similar orientation, but underwent 45°- anticlockwise rotation caused by the opening of the Liguro-Provençal Basin.

Finally, an overall decreasing trend of cooling ages is observed from the internal high-pressure regions toward the western ECM (Fig. 6) implying that exhumation first affected the internal units before progressively propagating toward the external units, (e.g. Fügenschuh and Schmid 2003). In the high-pressure regions, the minimal onset of exhumation (i.e. the maximal age of the start of exhumation) is constrained at ~36 Ma by fissure monazite (this study) and phengite crystallization (Agard et al. 2002) under greenschist facies conditions. These ages are older than ZFT cooling ages (Fig. 6), whereas in the western ECM the minimal onset of exhumation follows ZFT ages, and fissure monazite crystallization is systematically observed between ZFT and AFT cooling ages. These observations suggest slower cooling rates in the internal units with respect to the external ones.

5.3 Fissure monazite composition

The composition of fissure monazites provides hints on dissolved host-rock minerals and oxidation condition, in the fissure. Trace element analyses of fissure monazite show a negative Eu anomaly, most likely resulting from co-crystallization of albite. The difference in negative Eu/Eu* is interpreted to be inherited from the host rock and is distinct in VIU1 (Piemontais Zone) compared to the other grains (Fig. 4). Generally, the REE content of fissure monazite does not change systematically over time, but seems mainly controlled by dissolution of available REE-bearing accessory minerals.

The high Th/U content of the VINA1 grain indicates a strongly oxidizing environment of crystallization in association with hematite, as described by Gnos et al. (2015) (Fig. 5a). It has indeed been mentioned that hematite is not rare in fissures in this area (Piccoli 2002). Sr and Ca correlation indicates dissolution of host-rock plagioclase

or carbonate as a source (Gnos et al. 2015; Fig. 5b). Samples from the Argentera Massif (MORI1, VINA1 and GEES1) have nearly identical Sr/Ca ratios (average Sr/Ca = 0.22), suggesting a similar source for these elements. In contrast, samples from the high-pressure regions have average Sr/Ca = 0.39 (BALZI2) and 0.17 (VIU1). An increase in Ce correlated with a decrease in Y suggests that more monazite or allanite, $(Ce^{3+},La^{3+},Nd^{3+},Ca^{2+},Y^{3+})_2(Al^{3+},Fe^{2+},Fe^{3+})_3(SiO_4)_3(OH)$, was dissolved with respect to xenotime (Fig. 5c). Finally, an increase in cheralite component (Ca + Th replacing 2REE) related to a decrease of xenotime component (Y) is observed for grains VINA1 and VIU1 (Fig. 5). Only in few cases REE and trace elements show sufficient variation helping to separate growth domains in the hydrothermal monazites studied here. There is also no systematic compositional change over time.

6 Conclusions

The oldest ages recorded by fissure monazite found in the Briançonnais Zone are related to exhumation along the PF during top-NNW thrusting in sinistral transpression. This first exhumation episode was overprinted by subsequent top-WNW thrusting recorded between ~32 and 30 Ma in fissure monazites from the Briançonnais and Piemontais zones. During top-SW thrusting, fissure monazite crystallization is recorded in association with strike-slip faulting in the Briançonnais Zone Houillère at ~23 Ma, likely related to the progressive opening of the Liguro-Provençal Basin. Later, at ~20.6 Ma, fissure monazite from a fault zone located in the south-western border of the Argentera Massif is attributed to the onset of the anticlockwise rotation of the Corsica-Sardinia Block. By contrast, monazite crystallization recorded at ~16–14 Ma in a fault zone of the north-eastern Argentera Massif likely constrains the end of the Corsica-Sardinia block rotation. Contemporaneous with this rotation, deformation during the exhumation of the Pelvoux Massif is recorded at ~17.6 Ma. Finally, successively younger episodes of dextral strike-slip related to increasing concentration of deformation along the Rhone-Simplon/Penninic Front fault system are recorded at ~12–11 and ~8–5 Ma in the Belledonne Massif and at ~12–7 Ma in the Mont-Blanc and Aiguilles Rouges massifs, marking the jump from thrusting to dextral strike-slip faulting toward the northern ECM of the Western Alps.

Chemical observations of the investigated fissure monazites suggest a similar source of Sr and Ca for the grains from the Argentera Massif, generally higher amounts of monazite or allanite dissolution from the host-rock with respect to xenotime and corroborate previous

observations of extremely high Th/U content formed under oxidizing conditions.

Acknowledgements

We thank Gaspare Maletto, Roberto Bracco and Francis Guichon for providing the samples and valuable information on the sample localities. We also thank Daniel Marty and Paola Manzotti for the editing work as well as Neil Mancktelow and an anonymous reviewer for their helpful comments.

Authors' contributions

Fissure monazite samples were organized by EG and selected for ion probe dating by EG and ER according to tectonic settings and activity of the study area. Sample preparation and BSE imaging was carried out by ER. Ion probe and LA-ICP-MS data acquisition and reduction was performed by ER under the supervision of DR, MJW and TP respectively. The manuscript was prepared by ER during her PhD project under the supervision of EG with contributions from all co-authors. All authors read and approved the final manuscript.

Funding

This study was financed by the Swiss National Foundation Grant 200020–165513.

Availability of data and materials.

All data generated or analysed during this study are included in this published article and its additional files.

Competing interests

The authors declare that they have no competing interests.

Author details

¹ Department of Earth Sciences, University of Geneva, Rue des Maraîchers 13, 1205 Geneva, Switzerland. ² Natural History Museum of Geneva, Route de Malagnou 1, 1208 Geneva, Switzerland. ³ Institute of Geological Sciences, University of Bern, Baltzerstrasse 1+3, 3012 Bern, Switzerland. ⁴ Institute of Earth Sciences, University of Lausanne, 1015 Geopolis, Lausanne, Switzerland. ⁵ Swedish Museum of Natural History, Box 50007, 10405 Stockholm, Sweden.

Received: 4 April 2020 Accepted: 18 August 2020

Published online: 15 October 2020

References

- Agard, P., Monié, P., Jolivet, L., & Goffé, B. (2002). Exhumation of the Schistes Lustrés complex: In situ laser probe $^{40}\text{Ar}/^{39}\text{Ar}$ constraints and implications for the Western Alps. *Journal of Metamorphic Geology*, 20(6), 599–618. <https://doi.org/10.1046/j.1525-1314.2002.00391.x>.
- Aleinikoff, J. N., Schenck, W. S., Plank, M. O., Srogi, L. A., Fanning, C. M., Kamo, S. L., et al. (2006). Deciphering igneous and metamorphic events in high-grade rocks of the Wilmington complex, Delaware: Morphology, cathodoluminescence and backscattered electron zoning, and SHRIMP U-Pb geochronology of zircon and monazite. *Bulletin of the Geological Society of America*, 118(1–2), 39–64. <https://doi.org/10.1130/B25659.1>.
- Bellanger, M., Augier, R., Bellahsen, N., Jolivet, L., Monié, P., Baudin, T., et al. (2015). Shortening of the European dauphinois margin (Oisans Massif, Western Alps): New insights from RSCM maximum temperature estimates and $40\text{Ar}/39\text{Ar}$ in situ dating. *Journal of Geodynamics*, 83, 37–64. <https://doi.org/10.1016/j.jog.2014.09.004>.
- Bergemann, C. A., Gnos, E., Berger, A., Janots, E., & Whitehouse, M. J. (2020). Dating tectonic activity in the Lepontine Dome and Rhone-Simplon Fault regions through hydrothermal monazite-(Ce). *Solid Earth*, 199–222.
- Bergemann, C. A., Gnos, E., Berger, A., Whitehouse, M. J., Mullis, J., Walter, F., et al. (2018). Constraining long-term fault activity in the brittle domain through in situ dating of hydrothermal monazite. *Terra Nova*, 30(6), 440–446. <https://doi.org/10.1111/ter.12360>.
- Bergemann, C. A., Gnos, E., Berger, A., Whitehouse, M., Mullis, J., Wehren, P., et al. (2017). Th-Pb ion probe dating of zoned hydrothermal monazite and its implications for repeated shear zone activity: An example from the Central Alps, Switzerland. *Tectonics*, 36(4), 671–689. <https://doi.org/10.1002/2016TC004407>.
- Bergemann, C. A., Gnos, E., & Whitehouse, M. J. (2019). Insights into the tectonic history of the Western Alps through dating of fissure monazite in the Mont Blanc and Aiguilles Rouges Massifs. *Tectonophysics*, 750(2018), 203–212. <https://doi.org/10.1016/j.tecto.2018.11.013>.
- Berger, A., Gnos, E., Janots, E., Whitehouse, M., Soom, M., Frei, R., et al. (2013). Dating brittle tectonic movements with cleft monazite: Fluid-rock interaction and formation of REE minerals. *Tectonics*, 32(5), 1176–1189. <https://doi.org/10.1002/tect.20071>.
- Beucher, R. (2009). Evolution Néogène de l'arc alpin sud-occidental: Approches sismotectonique et thermochronologique.
- Beucher, R., Van Der Beek, P., Braun, J., & Batt, G. E. (2012). Exhumation and relief development in the Pelvoux and Dora-Maira massifs (western Alps) assessed by spectral analysis and inversion of thermochronological age transects. *Journal of Geophysical Research: Earth Surface*, 117(3), 1–22. <https://doi.org/10.1029/2011JF002240>.
- Bigot-Cormier, F., Sosson, M., Poupeau, G., Stéphan, J. F., & Labrin, E. (2006). The denudation history of the Argentera Alpine external crystalline massif (Western Alps, France-Italy): An overview from the analysis of fission tracks in apatites and zircons. *Geodinamica Acta*, 19(6), 455–473. <https://doi.org/10.3166/ga.19.455-473>.
- Bogdanoff, S., Michard, A., Mansour, M., & Poupeau, G. (2000). Apatite fission track analysis in the Argentera massif: Evidence of contrasting denudation rates in the external crystalline massifs of the Western Alps. *Terra Nova*, 12(2), 117–125. <https://doi.org/10.1111/j.1365-3121.2000.00281.x>.
- Bousquet, R., Oberhansli, R., Schmid, S., Berger, A., Wiederkehr, M., Robert, C., et al. (2012). *Metamorphic framework of the Alps: Map 1: 1 000 000. University of Basel*.
- Bracco, R., Balestra, C., Castellar, F., Mills, S. J., Ma, C., Callegari, A. M., et al. (2012). Nuovi minerali di Terre Rare da Costa Balzi Rossi, Maglioli (SV), Liguria. *Micro*, 10, 66–77.
- Campani, M., Mancktelow, N., Seward, D., Rolland, Y., Mueller, W., & Guerra, I. (2010). Geochronological evidence for continuous exhumation through the ductile-brITTLE transition along a crustal-scale low-angle normal fault: Simplon Fault Zone, central Alps. *Tectonics*. <https://doi.org/10.1029/2009TC002582>.
- Cardello, G. L., Di Vincenzo, G., Giorgetti, G., Zwingmann, H., & Mancktelow, N. (2019). Initiation and development of the Pennine Basal Thrust (Swiss Alps): a structural and geochronological study of an exhumed megathrust. *Journal of Structural Geology*, 126, 338–356.
- Carpéna, J. (1992). Fission-track dating of zircon: zircons from Mont-Blanc granite (French-Italian Alps). *The Journal of Geology*, 100, 411–421.
- Cenki-Tok, B., Darling, J. R., Rolland, Y., Dhuime, B., & Storey, C. D. (2014). Direct dating of mid-crustal shear zones with synkinematic allanite: New in situ U-Th-Pb geochronological approaches applied to the Mont Blanc massif. *Terra Nova*, 26(1), 29–37. <https://doi.org/10.1111/ter.12066>.
- Ceriani, S., Fügenschuh, B., & Schmid, S. M. (2001). Multi-stage thrusting at the "Penninic Front" in the Western Alps between Mont Blanc and Pelvoux massifs. *International Journal of Earth Sciences*, 90(3), 685–702. <https://doi.org/10.1007/s005310000188>.
- Cherniak, D. J., & Pyle, J. M. (2008). Th diffusion in monazite. *Chemical Geology*, 256(1–2), 52–61. <https://doi.org/10.1016/j.chemgeo.2008.07.024>.
- Cherniak, D. J., Watson, E. B., Grove, M., & Harrison, T. M. (2004). Pb diffusion in monazite: A combined RBS/SIMS study. *Geochimica et Cosmochimica Acta*, 68(4), 829–840. <https://doi.org/10.1016/j.gca.2003.07.012>.
- Collombet, M., Thomas, J. C., Chauvin, A., Tricart, P., Bouillin, J. P., & Gratier, J. P. (2002). Counterclockwise rotation of the western Alps since the Oligocene: New insights from paleomagnetic data. *Tectonics*, 21, 4. <https://doi.org/10.1029/2001TC001016>.
- Corsini, M., Ruffet, G., & Caby, R. (2004). Alpine and late-hercynian geochronological constraints in the Argentera Massif (Western Alps). *Ectogae Geologicae Helvetiae*, 97(1), 3–15. <https://doi.org/10.1007/500015-004-1107-8>.
- Crespo-Blanc, A., Masson, H., Sharp, Z., Cosca, M., & Hunziker, J. (1995). A stable and $^{40}\text{Ar}/^{39}\text{Ar}$ isotope study of a major thrust in the Helvetic Nappes (Swiss Alps): evidence for fluid flow and constraints on nappe kinematics. *Geological Society of America Bulletin*, 107(10), 1129–1144. [https://doi.org/10.1130/0016-7606\(1995\)107<1129:ASAAI>2.3.CO;2](https://doi.org/10.1130/0016-7606(1995)107<1129:ASAAI>2.3.CO;2).
- Crouzet, C., Ménard, G., & Rochette, P. (2001). Cooling history of the Dauphiné zone (Western Alps, France) deduced from the thermopaleomagnetic record: Geodynamic implications. *Tectonophysics*, 340(1–2), 79–93. [https://doi.org/10.1016/S0040-1951\(01\)00142-1](https://doi.org/10.1016/S0040-1951(01)00142-1).

- Dumont, T., Schwartz, S., Guillot, S., Simon-Labréteau, T., Tricart, P., & Jourdan, S. (2012). Structural and sedimentary records of the Oligocene revolution in the Western Alpine arc. *Journal of Geodynamics*, 56–57, 18–38. <https://doi.org/10.1016/j.jog.2011.11.006>.
- Egli, D., Mueller, W., & Mancktelow, N. (2016). Laser-cut Rb-Sr microsampling dating of deformational events in the Mont Blanc-Aiguilles Rouges region (European Alps). *Terra Nova*, 28, 35–42.
- Finello, G., Ambrino, P., Kolitsch, U., Ciriotti, M. E., Blass, G., & Bracco, R. (2007). I minerali della "Pietra di Luserna," Piemonte, Italia Nord-Orientale. I. Alcune cave di gneiss della Val Luserna. *MICRO*, 181–226.
- Fitz-Diaz, E., Cottle, J. M., Vidal-Reyes, M. I., & van der Pluijm, B. (2019). In situ Th/Pb dating of monazite in fibrous veins: Direct dating of veins and deformation in the shallow upper crust of the Mexican Orogen. *Journal of Structural Geology*, 124, 136–142. <https://doi.org/10.1016/j.jsg.2019.04.004>.
- Freeman, S. R., Butler, R. W. H., Cliff, R. A., Inger, S., & Barnicoat, A. C. (1998). Deformation migration in an orogen-scale shear zone array: An example from the Basal Briançonnais Thrust, internal Franco-Italian Alps. *Geological Magazine*, 135(3), 349–367. <https://doi.org/10.1017/S0016756898008693>.
- Freeman, S. R., Inger, S., Butler, R. W. H., & Cliff, R. A. (1997). Dating deformation using Rb-Sr in white mica: Greenschist facies deformation ages from the Entrelor shear zone Italian Alps. *Tectonics*, 16(1), 57–76. <https://doi.org/10.1029/96TC02477>.
- Fügenschuh, B., Loprieno, A., Ceriani, S., & Schmid, S. M. (1999). Structural analysis of the Subbriançonnais and Valais units in the area of Moûtiers (Savoy, Western Alps): paleogeographic and tectonic consequences. *International Journal of Earth Sciences*, 88(2), 201–218.
- Fügenschuh, B., & Schmid, S. M. (2003). Late stages of deformation and exhumation of an orogen constrained by fission-track data: A case study in the Western Alps. *Bulletin of the Geological Society of America*, 115(11), 1425–1440. <https://doi.org/10.1130/B25092.1>.
- Gardés, E., Jaoul, O., Montel, J. M., Seydoux-Guillaume, A. M., & Wirth, R. (2006). Pb diffusion in monazite: An experimental study of $Pb^{2+} + Th^{4+} \rightleftharpoons 2Nd^{3+}$ interdiffusion. *Geochimica et Cosmochimica Acta*, 70(9), 2325–2336. <https://doi.org/10.1016/j.gca.2006.01.018>.
- Gardés, E., Montel, J. M., Seydoux-Guillaume, A. M., & Wirth, R. (2007). Pb diffusion in monazite: New constraints from the experimental study of $Pb^{2+} + \rightleftharpoons Ca^{2+}$ interdiffusion. *Geochimica et Cosmochimica Acta*, 71(16), 4036–4043. <https://doi.org/10.1016/j.gca.2007.06.036>.
- Gasquet, D. (1979). *Etude pétrologique, géochimique et structurale des terrains cristallins de Belledonne et du Grand Chatelard traversés par les galeries EDF Arc-Isère-Alpes Françaises*.
- Gasquet, D., Bertrand, J. M., Paquette, J. L., Lehmann, J., Ratzov, G., Ascenção De Guedes, R. A., et al. (2010). Miocene to Messinian deformation and hydrothermal activity in a pre-Alpine basement massif of the French western Alps: New U-Th-Pb and argon ages from the Lauzière massif. *Bulletin de la Société Géologique de France*, 181(3), 227–241. <https://doi.org/10.2113/gssgbull.181.3.227>.
- Gattacceca, J., Deino, A., Rizzo, R., Jones, D. S., Henry, B., Beaudoin, B., et al. (2007). Miocene rotation of Sardinia: New paleomagnetic and geochronological constraints and geodynamic implications. *Earth and Planetary Science Letters*, 258(3–4), 359–377. <https://doi.org/10.1016/j.epsl.2007.02.003>.
- Glötzbach, C., Reinecker, J., Danišák, M., Rahn, M., Frisch, W., & Spiegel, C. (2010). Thermal history of the central Gotthard and Aar massifs, European Alps: Evidence for steady state, long-term exhumation. *Journal of Geophysical Research: Earth Surface*, 115(3), F03017. <https://doi.org/10.1029/2009JF001304>.
- Glötzbach, C., van der Beek, P. A., & Spiegel, C. (2011). Episodic exhumation and relief growth in the Mont Blanc massif, Western Alps from numerical modelling of thermochronology data. *Earth and Planetary Science Letters*, 304(3–4), 417–430. <https://doi.org/10.1016/j.epsl.2011.02.020>.
- Gnos, E., Janots, E., Berger, A., Whitehouse, M., Walter, F., Pettke, T., et al. (2015). Age of cleft monazites in the eastern Tauern Window: constraints on crystallization conditions of hydrothermal monazite. *Swiss Journal of Geosciences*, 108(1), 55–74. <https://doi.org/10.1007/s00015-015-0178-z>.
- Grand'Homme, A., Janots, E., Bosse, V., Seydoux-Guillaume, A. M., & Ascenção De Guedes, R. A. (2016a). Interpretation of U-Th-Pb in-situ ages of hydrothermal monazite-(Ce) and xenotime-(Y): evidence from a large-scale regional study in clefts from the western alps. *Mineralogy and Petrology*, 110(6), 787–807. <https://doi.org/10.1007/s00711-016-0451-5>.
- Grand'Homme, A., Janots, E., Seydoux-Guillaume, A. M., Guillaume, D., Bosse, V., & Magnin, V. (2016b). Partial resetting of the U-Th-Pb systems in experimentally altered monazite: Nanoscale evidence of incomplete replacement. *Geology*, 44(6), 431–434. <https://doi.org/10.1130/G37770.1>.
- Grand'Homme, A., Janots, E., Seydoux-Guillaume, A.-M., Guillaume, D., Magnin, V., Hövelmann, J., et al. (2018). Mass transport and fractionation during monazite alteration by anisotropic replacement. *Chemical Geology*, 484, 51–68. <https://doi.org/10.1016/j.chemgeo.2017.10.008>.
- Grasemann, B., & Mancktelow, N. S. (1993). Two-dimensional thermal modeling of normal faulting: the Simplon Fault Zone, Central Alps, Switzerland. *Tectonophysics*, 225, 155–165.
- Gray, A. L. (1985). Solid sample introduction by laser ablation for inductively coupled plasma source mass spectrometry. *Analyst*, 110, 551–556.
- Guillong, M., Meier, D. L., Allan, M. M., & Heinrich, C. A. (2008). SILLS: a MATLAB-based program for the reduction of laser ablation ICP-MS data of homogeneous materials and inclusions. In P. J. Sylvester (Ed.), *Laser ablation ICP-MS in the Earth Sciences: Current practices and outstanding issues* (pp. 328–333). Mineralogical Association of Canada Short Course Series: Toronto.
- Hubbard, M., & Mancktelow, N. S. (1992). Lateral displacement during Neogene convergence in the western and central Alps. *Geology*, 20(10), 943–946. [https://doi.org/10.1130/0091-7613\(1992\)020<0943:LLDNCI>2.3.CO;2](https://doi.org/10.1130/0091-7613(1992)020<0943:LLDNCI>2.3.CO;2).
- Janots, E., Berger, A., Gnos, E., Whitehouse, M., Lewin, E., & Pettke, T. (2012). Constraints on fluid evolution during metamorphism from U-Th-Pb systematics in Alpine hydrothermal monazite. *Chemical Geology*, 326, 61–71.
- Janots, E., Grand'Homme, A., Bernet, M., Guillaume, D., & Gnos, E. (2019). Geochronological and thermometric evidence of unusually hot fluids in an Alpine fissure of Lauzière granite (Belledonne, Western Alps). *Solid Earth*, 10(1), 211–223.
- Kirschner, D. L., Masson, H., & Cosca, M. A. (2003). An $^{40}\text{Ar}/^{39}\text{Ar}$, Rb/Sr, and stable isotope study of micas in low-grade fold-and-thrust belt: An example from the Swiss Helvetic Alps. *Contributions to Mineralogy and Petrology*, 145(4), 460–480. <https://doi.org/10.1007/s00410-003-0461-2>.
- Lanari, P., Rolland, Y., Schwartz, S., Vidal, O., Guillot, S., Tricart, P., et al. (2014). P-T-t estimation of deformation in low-grade quartz-feldspar-bearing rocks using thermodynamic modelling and $^{40}\text{Ar}/^{39}\text{Ar}$ dating techniques: Example of the Plan-de-Phasys shear zone unit (Briançonnais Zone, Western Alps). *Terra Nova*, 26(2), 130–138. <https://doi.org/10.1111/ter.12079>.
- Laubscher, H. (1991). The arc of the Western Alps today. *Eclogae Geologicae Helveticae*, 84(3), 359–631.
- Lelarge, M. L. (1993). Thermochronologie par la méthode des traces de fission d'une marge passif(Dôme de Ponta Grossa, Se Bresil) et au sein d'une chaîne de collision (Zone externe del'arc alpin, France). *PhD thesis, Université Joseph Fourier Grenoble, Franc*.
- Leloup, P. H., Arnaud, N., Sobel, E. R., & Lacassin, R. (2005). Alpine thermal and structural evolution of the highest external crystalline massif: The Mont Blanc. *Tectonics*, 24(4), 1–26. <https://doi.org/10.1029/2004TC001676>.
- Lemoine, M., Bas, T., Arnaud-Vanneau, A., Arnaud, H., Dumont, T., Gidon, M., et al. (1986). The continental margin of the Mesozoic Tethys in the Western Alps. *Marine and Petroleum Geology*, 3(3), 179–199. [https://doi.org/10.1016/0264-8172\(86\)90044-9](https://doi.org/10.1016/0264-8172(86)90044-9).
- Leutwein, F., Poty, B., Sonet, J., & Zimmerman, J. L. (1970). Age des cavités à cristaux du granite du Mont Blanc. *Acad. Sci. Paris*, 271, 156–158.
- Ludwig, K. R. (2003). User's manual for a geochronological toolkit for Microsoft Excel (Isoplots/Ex version 3.0). *Berkeley Geochronol. Cent. Spec. Publ.*, 4, 1–70.
- Maffione, M., Speranza, F., Faccenna, C., Cascella, A., Vignaroli, G., & Sagnotti, L. (2008). A synchronous Alpine and Corsica-Sardinia rotation. *Journal of Geophysical Research: Solid Earth*, 113(3), 1–25. <https://doi.org/10.1029/2007JB005214>.
- Malusà, M. G., Polino, R., Zattin, M., Bigazzi, G., Martin, S., & Piana, F. (2005). Miocene to Present differential exhumation in the Western Alps: Insights from fission track thermochronology. *Tectonics*, 24(3), 1–23. <https://doi.org/10.1029/2004TC001782>.
- Malusà, M. G., & Vezzoli, G. (2006). Interplay between erosion and tectonics in the western alps: interplay between erosion and tectonics. *Terra Nova*, 18(2), 104–108. <https://doi.org/10.1111/j.1365-3121.2006.00669.x>.

- Mancktelow, N. S. (1992). Neogene lateral extension during convergence in the Central Alps: Evidence from interrelated faulting and backfolding around the Simplonpass (Switzerland). *Tectonophysics*, 215, 295–317.
- Markley, M. J., Teyssier, C., Cosca, M. A., Caby, R., Hunziker, J. C., & Sartori, M. (1998). Alpine deformation and $^{40}\text{Ar}/^{39}\text{Ar}$ geochronology of synkinematic white mica in the Siviez-Michael Nappe, western pennine Alps, Switzerland. *Tectonics*, 17, 407–425.
- Marshall, D., Pfeifer, H.-R., Hunziker, J. C., & Kirschner, D. (1998). A pressure-temperature-time path for the NE Mont-Blanc massif: Fluid-inclusion, isotopic and thermobarometric evidence. *European Journal of Mineralogy*, 10(6), 1227–1240. <https://doi.org/10.1127/ejm/10/6/1227>.
- McDonough, W. F., & Sun, S. S. (1995). The composition of the Earth. *Chemical Geology*, 120(3–4), 223–253. [https://doi.org/10.1016/0012-821X\(95\)00123-T](https://doi.org/10.1016/0012-821X(95)00123-T).
- McLennan, S. M. (1989). Rare earth elements in sedimentary rocks: influence of provenance and sedimentary processes. *Geochemistry and Mineralogy of Rare Earth Elements, Reviews in Mineralogy*, 21, 169–200.
- Mullis, J. (1996). P-T-t path of quartz formation in extensional veins of the Central Alps. *Schweizerische Mineralogische und Petrographische Mitteilungen*, 76, 159–164. <https://doi.org/10.5169/seals-57694>.
- Pettke, T., Oberli, F., Audet, A., Guillong, M., Simon, A. C., Hanley, J. J., et al. (2012). Recent developments in element concentrations and isotope ratio analysis of individual fluid inclusions by laser ablation single and multiple collector ICP-MS. *Ore Geology Reviews*, 44, 10–38.
- Piccoli, G. C. (2002). *Minerali delle Alpi Marittime e Cozie*. Provincia di Cuneo: L'Artistica Savigliano.
- Ricchi, E., Bergemann, C. A., Gnos, E., Berger, A., Rubatto, D., & Whitehouse, M. J. (2019). Constraining deformation phases in the Aar Massif and the Gotthard Nappe (Switzerland) using Th-Pb crystallization ages of fissure monazite-(Ce). *Lithos*, 342–343, 223–238. <https://doi.org/10.1016/j.lithos.2019.04.014>.
- Ricchi, E., Bergemann, C. A., Gnos, E., Berger, A., Rubatto, D., Whitehouse, M. J., et al. (2020). Cenozoic deformation in the Tauern Window (Eastern Alps) constrained by in situ Th-Pb dating of fissure monazite. *Solid Earth*, 11(437–467), 2020. <https://doi.org/10.5194/se-11-437-2020>.
- Rolland, Y., Rossi, M., Cox, S. F., Corsini, M., Mancktelow, N., Pennacchioni, G., et al. (2008). 40 Ar / 39 Ar dating of synkinematic white mica: insights from fluid-rock reaction in low-grade shear zones (Mont Blanc Massif) and constraints on timing of deformation in the NW external Alps. *Geological Society, London, Special Publications*, 299(1), 293–315. <https://doi.org/10.1144/sp299.18>.
- Rossi, M., & Rolland, Y. (2014). Stable isotope and Ar/Ar evidence of prolonged multiscale fluid flow during exhumation of orogenic crust: Example from the mont blanc and Aar Massifs (NW Alps). *Tectonics*, 33(9), 1681–1709. <https://doi.org/10.1002/2013TC003438>.
- Rubatto, D., Gebauer, D., & Compagnoni, R. (1999). Dating of eclogite-facies zircons: The age of Alpine metamorphism in the Sesia-Lanzo Zone (Western Alps). *Earth and Planetary Science Letters*, 167(3–4), 141–158. [https://doi.org/10.1016/S0012-821X\(99\)00031-X](https://doi.org/10.1016/S0012-821X(99)00031-X).
- Rubatto, D., & Hermann, J. (2001). Exhumation as fast as subduction? *Geology*, 29(1), 3–6.
- Rubatto, D., & Hermann, J. (2003). Zircon formation during fluid circulation in eclogites (Monviso, Western Alps): Implications for Zr and Hf budget in subduction zones. *Geochimica et Cosmochimica Acta*, 67(12), 2173–2187.
- Sabil, N. (1995). La datation par traces de fission : aspects méthodologiques et applications thermochronologiques en contexte alpin et de marge continentale., 238.
- Sanchez, G., Rolland, Y., Jolivet, M., Brichau, S., Corsini, M., & Carter, A. (2011a). Exhumation controlled by transcurrent tectonics: The Argentera-Mercantour massif (SW Alps). *Terra Nova*, 23(2), 116–126. <https://doi.org/10.1111/j.1365-3121.2011.00991.x>.
- Sanchez, G., Rolland, Y., Schneider, J., Corsini, M., Oliot, E., Goncalves, P., et al. (2011b). Dating low-temperature deformation son white mica, insights from the Argentera-Mercantour Massif (SW Alps). *Lithos*, 125(1–2), 521–536. <https://doi.org/10.1016/j.lithos.2011.03.009>.
- Schmid, S. M., Fügenschuh, B., Kissling, E., & Schuster, R. (2004). Tectonic map and overall architecture of the Alpine orogen. *Elogiae Geologicae Helvetiae*, 97(1), 93–117. <https://doi.org/10.1007/s00015-004-1113-x>.
- Schmid, S. M., Kissling, E., Diehl, T., van Hinsbergen, D. J. J., & Moll, G. (2017). Ivrea mantle wedge, arc of the Western Alps, and kinematic evolution of the Alps-Apennines orogenic system. *Swiss Journal of Geosciences*, 110(2), 581–612. <https://doi.org/10.1007/s00015-016-0237-0>.
- Schwartz, S., Lardeaux, J. M., Tricart, P., Guillot, S., & Labrin, E. (2007). Diachronous exhumation of HP-LT metamorphic rocks from south-western Alps: Evidence from fission-track analysis. *Terra Nova*, 19(2), 133–140. <https://doi.org/10.1111/j.1365-3121.2006.00728.x>.
- Schwartz, Stéphane. (2000). *La zone piémontaise des Alpes occidentales : un paléocomplexe de subduction. Arguments métamorphiques, géochronologiques et structuraux*. PhD Thesis. Université Claude Bernard, Lyon, France.
- Seward, D., & Mancktelow, N. S. (1994). Neogene kinematics of the central and western Alps: evidence from fission-track dating. *Geology*, 22(9), 803–806. [https://doi.org/10.1130/0091-7613\(1994\)022<0803:NKOTC>2.3.CO;2](https://doi.org/10.1130/0091-7613(1994)022<0803:NKOTC>2.3.CO;2).
- Seward, D., Ford, M., Bürgisser, J., Lickorish, H., Williams, E. A., & Meckel, L. D., III. (1999). Preliminary results of fission-track analyses in the southern Pelvoux area, SE France. *Memorie di Scienze Geologiche Padova*, 51, 25–31.
- Seydoux-Guillaume, A. M., Montel, J. M., Bingen, B., Bosse, V., de Parseval, P., Paquette, J. L., et al. (2012). Low-temperature alteration of monazite: Fluid mediated coupled dissolution-precipitation, irradiation damage, and disturbance of the U-Pb and Th-Pb chronometers. *Chemical Geology*, 330–331, 140–158. <https://doi.org/10.1016/j.chemgeo.2012.07.031>.
- Seydoux-Guillaume, A. M., Paquette, J. L., Wiedenbeck, M., Montel, J. M., & Heinrich, W. (2002). Experimental resetting of the U-Th-Pb systems in monazite. *Chemical Geology*, 191(1–3), 165–181. [https://doi.org/10.1016/S0009-2541\(02\)00155-9](https://doi.org/10.1016/S0009-2541(02)00155-9).
- Sharp, Z. D., Masson, H., & Lucchini, R. (2005). Stable isotope geochemistry and formation mechanisms of quartz veins; extreme paleoaltitudes of the Central Alps in the Neogene. *American Journal of Science*, 305(3), 187–219. <https://doi.org/10.2475/ajs.305.3.187>.
- Simon-Labric, T., Rolland, Y., Dumont, T., Heymes, T., Authemayou, C., Corsini, M., et al. (2009). $^{40}\text{Ar}/^{39}\text{Ar}$ dating of Penninic Front tectonic displacement (W Alps) during the Lower Oligocene (31–34 Ma). *Terra Nova*, 21(2), 127–136. <https://doi.org/10.1111/j.1365-3121.2009.00865.x>.
- Soom, M. (1990). *Abkühlungs- und Hebungsgeschichte der Externmassive und der Penninischen Decken beidseits der Simplon-Rhone-Linie seit dem Oligozän: Spaltspurdatierungen an Apatit/Zirkon und K/Ar Datierungen an Biotit/Muskowit (westliche Zentralalpen)*. PhD thesis, Universität Bern, Switzerland.
- Stacey, J. S., & Kramers, J. D. (1975). Approximation of terrestrial lead isotope evolution by a two-staged model. *Earth and Planetary Science Letters*, 26, 207–221.
- Stalder, H. A., Wagner, A., Graeser, S., & Stuker, P. (1998). *Mineralienlexikon der Schweiz*. (Wepf, Ed.). Wepf, Basel.
- Steck, A., Della Torre, F., Keller, F., Pfeifer, H. R., Hunziker, J., & Masson, H. (2013). Tectonics of the Lepontine Alps: ductile thrusting and folding in the deepest tectonic levels of the Central Alps. *Swiss Journal of Geosciences*, 106(3), 427–450.
- Steck, A., & Hunziker, J. (1994). The Tertiary structural and thermal evolution of the Central Alps: compressional and extensional structures in an orogenic belt. *Tectonophysics*, 238, 229–254.
- Strzerynski, P., Guillot, S., Leloup, P. H., Arnaud, N., Vidal, O., Ledru, P., et al. (2012). Tectono-metamorphic evolution of the Briançonnais zone (Modane-Aussois and Southern Vanoise units, Lyon Turin transect, Western Alps). *Journal of Geodynamics*, 56–57, 55–75. <https://doi.org/10.1016/j.jog.2011.11.010>.
- Sue, C., Thouvenot, F., Fréchet, J., & Tricart, P. (1999). Widespread extension in the core of the western Alps revealed by earthquake analysis. *Journal of Geophysical Research: Solid Earth*, 104(B11), 25611–25622.
- Tricart, P., Van Der Beek, P., Schwartz, S., & Labrin, E. (2007). Diachronous late-stage exhumation across the western Alpine arc: constraints from apatite fission-track thermochronology between the Pelvoux and Dora-Maira Massifs. *Journal of the Geological Society*, 164(1), 163–174.
- van der Beek, P. A., Valla, P. G., Herman, F., Braun, J., Persano, C., Dobson, K. J., et al. (2010). Inversion of thermochronological age-elevation profiles to extract independent estimates of denudation and relief history - II: Application to the French Western Alps. *Earth and Planetary Science Letters*, 296(1–2), 9–22. <https://doi.org/10.1016/j.epsl.2010.04.032>.

- Vance, J. (1999). Zircon fission track evidence for a Jurassic (Tethyan) thermal event in the western alps. *Memorie di Scienze Geologiche, Padova*, 51(2), 473–476.
- Villa, I. M., Bucher, S., Bousquet, R., Kleinhanns, I. C., & Schmid, S. M. (2014). Dating polygenetic metamorphic assemblages along a transect across the western alps. *Journal of Petrology*, 55(4), 803–830. <https://doi.org/10.1093/petrology/egu007>.

Publisher's Note

Springer Nature remains neutral with regard to jurisdictional claims in published maps and institutional affiliations.

Submit your manuscript to a SpringerOpen® journal and benefit from:

- Convenient online submission
- Rigorous peer review
- Open access: articles freely available online
- High visibility within the field
- Retaining the copyright to your article

Submit your next manuscript at ► springeropen.com
